Mode-Locking a Longitudinally Pumped Low Pressure Atomic Iodine Laser

By

Kenneth S. Gurley

B.S., United States Air Force Academy, 1984

THESIS

Submitted in Partial Fulfillment of the
Requirements for the Degree of
Master of Science in Physics

The University of New Mexico
Albuquerque, New Mexico

July, 1994

ACKNOWLEDGMENTS

This work is funded by the United States Air Force and was performed at the Chemical Laser Facility located at the Air Force Phillips Laboratory, Kirtland Air Force Base New Mexico. Thanks also to the Air Force Institute of Technology (AFIT), who, in conjunction with the United States Air Force Academy have graciously allowed the two years for me to concentrate on obtaining a Master's Degree in Physics.

Dr. Jack McIver has been my academic and research advisor from the start of my entrance into the University of New Mexico. Jack went out on a limb early to let me come to the lab and observe everyone there when I was really only qualified to take out the trash. I truly am in your debt for that. Thanks also for the most difficult class I have ever taken at UNM. I am only sorry that the concept of listing objectives and testing them has been clear only in your class.

Dr. Gordon Hager of the Phillips Laboratory has been the technical director of my project from its inception. I especially enjoyed his enthusiasm towards the scientific research conducted by myself and others at the lab. I have often said that, if Gordon had a month off from the lab, he would need a new staff of a thousand researchers to tackle all the projects he had dreamt up during that time. Thanks for sharing with me the incredible background knowledge you have on the Iodine atom. By the way, I have included your favorite picture if you have not drawn it yourself in the last few minutes.....

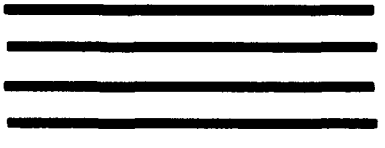

REPORT DOCUMENTATION PAGE

Form Approved
OMB No 0704-0188

1. AGENCY USE ONLY (Leave blank)	2. REPORT DATE	3. REPORT TYPE AND DATES COVERED
		THESIS/~~DISSERTATION~~

4. TITLE AND SUBTITLE Mode-Locking a Longitudinally Pumped Low Pressure Atomic Iodine Laser

5. FUNDING NUMBERS

6. AUTHOR(S)

Kenneth S. Gurley

7. PERFORMING ORGANIZATION NAME(S) AND ADDRESS(ES)

AFIT Student Attending:

University of New Mexico

8. PERFORMING ORGANIZATION REPORT NUMBER

AFIT/CI/CIA-

94-052

9. SPONSORING/MONITORING AGENCY NAME(S) AND ADDRESS(ES)

DEPARTMENT OF THE AIR FORCE
AFIT/CI
2950 P STREET
WRIGHT-PATTERSON AFB OH 45433-7765

10. SPONSORING/MONITORING AGENCY REPORT NUMBER

11. SUPPLEMENTARY NOTES

12a. DISTRIBUTION/AVAILABILITY STATEMENT

Approved for Public Release IAW 190-1
Distribution Unlimited
MICHAEL M. BRICKER, SMSgt, USAF
Chief Administration

12b. DISTRIBUTION CODE

13. ABSTRACT (Maximum 200 words)

74pp

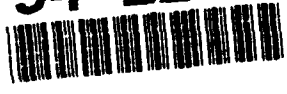

14. SUBJECT TERMS	15. NUMBER OF PAGES 67
	16. PRICE CODE

17. SECURITY CLASSIFICATION OF REPORT	18. SECURITY CLASSIFICATION OF THIS PAGE	19. SECURITY CLASSIFICATION OF ABSTRACT	20. LIMITATION OF ABSTRACT

Dr. Harold Miller is a visiting research scientist (IPA with JILA) from the University of Colorado at Boulder. Harold has been, for me, the ultimate devil's advocate. Though frustrating at times, I would have it no other way. You have pushed me to search for some answers with great diligence, if only just to prove you wrong. It has led me to a greater understanding of what I am doing. Thanks! By the way, I will let you know when you are wrong.....if that ever happens.

Lt. Scott Hunt has been my most valuable asset at the lab. Scott has been for me the ultimate source of "corporate knowledge" in my attempts to start and complete this project. Scott graciously helped me to learn all the pitfalls in assembling my setup without having to experience them. Thank you, Scott. It could not have been done in the time allotted without your help.

Ralph Tate, the consummate action man, is the liaison for the University of New Mexico and the chemical laser facility at Phillips Lab and has been a tremendous help in the lab. From what I understand, Ralph has forever been and forever shall be involved at the lab. His skills and abilities to put together a project in a short time are unmatched. Hesitation is not in Ralph's vocabulary. Ralph you should have been a fighter pilot...or, at the very least, worked for NIKE.....you know the "Just Do It" company.

Brain Anderson is a research physicist and "Shell Answer Man" at the Chemical Laser Facility. Brian, from the start, has been my sounding board for a plethora of silly, stupid, but sometimes pertinent lab questions. I thank you for being a good friend and not laughing in my general direction when the answers were quite simple.

And finally, I would also like to thank SSgt Phil Sanchez and Marty Viaz for completing the multitude of odd jobs and favors I asked of them. Not once did either balk at the chance to help me when I asked.

Mode-Locking a Longitudinally Pumped Low Pressure Atomic Iodine Laser

By

Kenneth S. Gurley

ABSTRACT OF THESIS

Submitted in Partial Fulfillment of the
Requirements for the Degree of

Master of Science in Physics

The University of New Mexico
Albuquerque, New Mexico

July, 1994

MODE-LOCKING A LONGITUDINALLY PUMPED LOW PRESSURE ATOMIC IODINE LASER

KENNETH SCOTT GURLEY
B.S., United States Air Force Academy, 1984
M.S., University of New Mexico, 1994

This paper describes the process leading up to and including the mode locking of a gain switched, photolytic iodine laser of low pressures < 30 Torr. First, prior to mode locking, the laser is characterized via output energy, pulse shape cavity buildup time and transverse and longitudinal mode structures. Second, the gain on the strongest transition line is measured two ways: directly with a narrowed source of tunable 1.3 mm coherent light from a solid state diode laser; and indirectly using energy absorption arguments and gain probe dimensions.

Finally, the laser is mode locked through active intracavity modulation with an acousto-optic modulator. Experimental data of minimum pulse width versus pressure are analyzed in detail.

TABLE OF CONTENTS

LIST OF FIGURES

1. INTRODUCTION

The purpose of this project is to serve as a test bed for mode locking at very low pressures. It is hoped that the results can be applied directly to mode locking a COIL (chemical oxygen iodine laser) device which typically operates at very low pressures within the exit region of its supersonic nozzles. This thesis describes theoretical and experimental results to achieve this goal.

The system to be tested is a mode locked, longitudinally pumped, gain switched, photolytic iodine laser operating at 1.315 μm. A KrF (krypton fluoride) excimer laser operating at 248 nm, produces an 18-20 ns pump pulse which is directed longitudinally into a cell containing CF_3I at pressures from 2 - 30 Torr. The CF_3I absorbs the ultraviolet (UV) light during the photolysis event and produces I* (or $^2P_{1/2}$) in a time short by comparison to the mode build up time. The upper state of atomic iodine is spilt into two hyperfine levels and the population is distributed statistically there [1]. The other lower energy fine structure state, I or $^2P_{3/2}$, is split into four hyperfine levels. Magnetic dipole transitions are allowed between the upper and lower hyperfine states. Magnetic dipole selection rules give 6 radiative transitions between the hyperfine levels with the 3-4 (from the $^2P_{1/2}$, $\overline{F} = 3$ to the $^2P_{3/2}$, $\overline{F} = 4$) being the strongest. Numerous processes act upon the inverted population with the cavity as the stimulated signal builds out of statistical noise. The radiative processes include the original pump pulse, spontaneous emission, and stimulated emission. The non-radiative processes include hyperfine relaxation, quenching, recombination and dimerization. While the radiative and non-radiative processes occur, an intracavity loss modulator selectively provides loss at a frequency equal to c/2L, where c is

the speed of light and L is the cavity length. The effect is, that during buildup of energy within the laser, various longitudinal modes are brought into a constant phase relationship. The summed effect of various intracavity frequencies is an output train of pulses spaced by c/2L whose width is relatively narrow. The ultimate pulse width is limited by the modulator's ability to provide loss, the gain bandwidth, and the type of broadening (homogenous or inhomogenous) that the gain experiences.

Chapter two of the text will explore the details of the theory involved in all the above mentioned processes. A short review of the atomic energy structure and its radiative and non-radiative process will be given. The emphasis in this chapter will be placed on mode locking theory and its relationship to this thesis.

Chapter three gives a detailed outline of the experiment. The equipment used and its limitations will be discussed. The overall layout of the experimental laser and associated test equipment will be presented. The details of data acquisition and associated problems will also be discussed.

Chapter four will first include a discussion of the characteristics of the excimer pumped photolytic iodine laser prior to mode locking it. Information regarding the characteristics of the mode locked laser system will get the most attention. The associated error analysis will be presented with each piece of data shown.

Conclusions will be drawn in chapter five for the project with regards to original objectives.

Finally, in chapter six, suggestions to improve this experiment and to study new areas will be presented.

2. THEORY

2.1 Historical Review and Direction of Theory

To date, extensive research literature has accumulated concerning the atomic iodine laser. This research is motivated due to excited iodine's (I^* or $^2P_{1/2}$) ability to lase at a wavelength (λ) of 1.315 μm between hyperfine energy levels. The resultant infrared output has been thoroughly studied and used in many experiments including fusion oriented plasma experiments with the Asterix III/IV laser at the Max-Plank-Institute for Quantenoptic (MPQ), Garching [2]

To obtain excited iodine and employ it as a gain medium, many alkyl iodides have been tested in concert with various pumping schemes. Here is a partial list of the more important gain media that can be excited via photolysis to obtain I^*

Media[3]	Pump Source Type [4]
CF_3I	Flash Lamps
C_2F_5I	Open High Current Discharge
C_3F_7I	Excimer Light Sources
C_4F_9I [5]	

Despite the extensive amount of photolysis I* research, very little work has taken place at very low pressures. To date, most, if not all, research into mode locking an I* laser has taken place at 80 Torr [6] or above and usually is accompanied by a buffer gas to

assist in pressure broadening the gain spectrum. This project, however, will serve as a photolytic test bed for mode locking at very low pressures where inhomogenous gain broadening is dominate.

2.2 Energy Structure of Atomic Iodine

The energy structure of atomic iodine has been extensively studied [7]. Typical quantum mechanical analysis involves combining the L·S Coupling scheme with the nuclear spin (I=5/2) to quantify the hyperfine structure. Figure 2-1 represents the fine and hyperfine structure of atomic iodine in units of wave numbers (cm^{-1}).

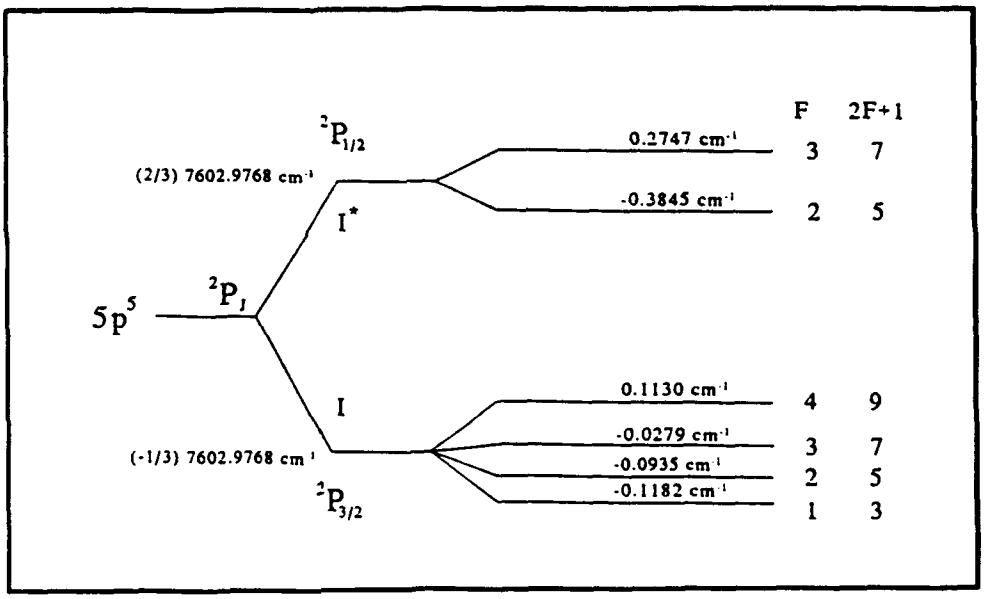

Figure 2-1 "Atomic Iodine Energy Levels"

RADIATIVE TRANSITIONS

In general, the electromagnetic field produced by an atom can be written as a series expansion of the electrical and magnetic multipole terms, each of which has its own

characteristic field pattern [8]. It has been shown that these characteristic multipoles and their fields obey selection rules based on the parity of the initial and final states of π_a (Parity of the Atomic State) and π_r (Parity of the Radiation Field). The result of the selection rules is to define a set of possible multipole order radiative transitions between the $^2P_{1/2}$ and the $^2P_{3/2}$ states. In principle, magnetic dipole, electric quadrupole, magnetic octopole and higher order multipoles are all possible [9], but the magnetic dipole transition dominates. Using the $\Delta F = 0, \pm 1$ selection rule (where F is the total angular momentum), the six allowable transitions are shown in Figure 2-2 matched with their associate spectrum data.

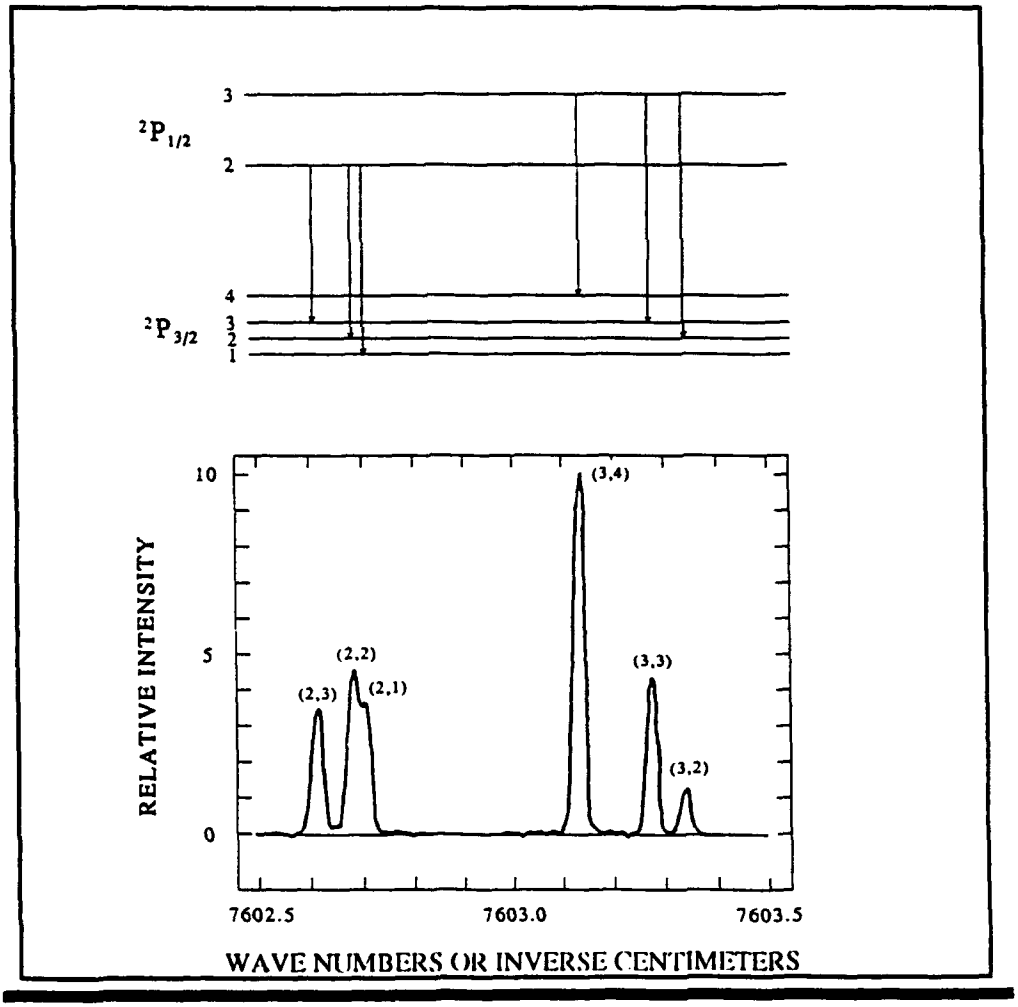

Figure 2-2 "Allowable Transitions and Spectrum Data"

The possible radiative transitions will have a relative intensity proportional to their

respective A (Einstein) coefficients for the transition of interest. The A-coefficient for the magnetic dipole radiative transition, A_{M1} can be written [10]

$$A_{M1} = A[_{initial,final}] = \frac{4k^3\mu_B^2}{3h}\left|\langle \psi_{final}|\hat{\mu}|\psi_{initial}\rangle\right|^2 \qquad [2.2\text{-}4]$$

where k = Wave Vector
h = Planck's Constant
μ_B = Bohr Magneton
$\hat{\mu}$ = Electric Dipole Moment Operator
ψ = Wave Function at Respective State

The resultant A-Coefficients with relative intensity for the allowed transitions [11] are

Transition	A-Coefficient	Normalized Intensity
2-3	2.46	0.346
2-2	3.07	0.432
2-1	2.37	0.333
3-4	5.08	1.000
3-3	2.20	0.433
3-2	0.63	0.124

Figure 2-3 "Einstein A-Coefficients in sec^{-1}"

2.3 Laser Processes

I* PRODUCTION

With the energy structure of atomic iodine known, it is time to backtrack and look at the mechanism which produces I* and with what efficiency that occurs. During

photolysis, one photon of UV light is absorbed and the effect can be represented by the following equation

$$CF_3I + h\upsilon_{248\ nm} \rightarrow CF_3 + I^* \qquad [2.3\text{-}1]$$

At 248 nm the cross section of absorption σ is $3x10^{-18}$ cm^2 for CF_3I [12]. Measured values of quantum yield for this process approach 100% [13] and will be assumed as such for the purposes of this text.

Once the I* is created, numerous other processes act upon it within the laser cavity. These processes include hyperfine relaxation, quenching, recombination, dimerization, and spontaneous and stimulated emission. Figure 2-4 is a pictorial representation of the above mentioned processes.

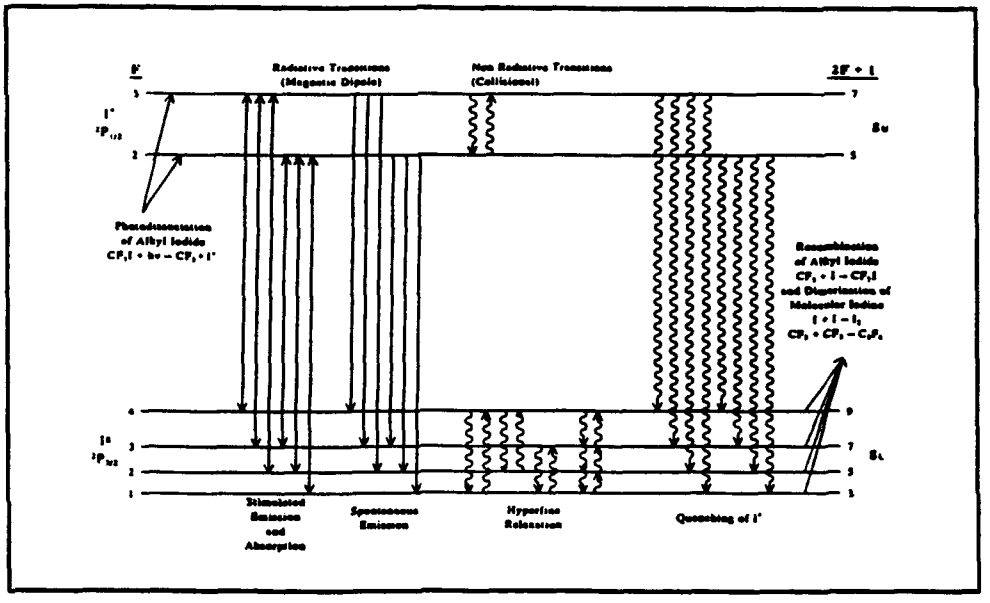

Figure 2-4 "Kinetic Processes in an Atomic Iodine Laser"

One only needs to include all events of interest in a rate equation model to determine the population of I* as a function of time. With the population of I* known, the output of the

laser can be determined. The rate equations for each hyperfine level and associated circulating intensity equations are listed in appendices 8.1 & 8.2 and have been incorporated into a computer model [14]. This model simulates a pulsed photolytic laser and will be referenced throughout this text.

2.4 Mode Locking Theory

The basic principle of mode locking can be illustrated in the summing of multiple electric fields each with an individual complex field of

$$E(t) = Ee^{j(\omega t+\phi)} \qquad [2.4\text{-}1]$$

where ω is the frequency, ϕ is the phase factor, j =-i, and E is the complex amplitude. The most obvious case to start with is the summing of two waves in the frequency domain. The output electric field is

$$E(t) = \mathrm{Re}[E_1 e^{j(\omega_1 t+\phi_1)} + E_2 e^{j(\omega_2 t+\phi_2)}] \qquad [2.4\text{-}2]$$

After taking the real part and squaring, the intensity is given by

$$I(t) = |E(t)|^2 = E_1^2 + E_2^2 + 2E_1E_2\cos[(\omega_2-\omega_1)t+\phi_2-\phi_1] \qquad [2.4\text{-}3]$$

This is illustrated, for equal amplitudes, by Figure 2-5.

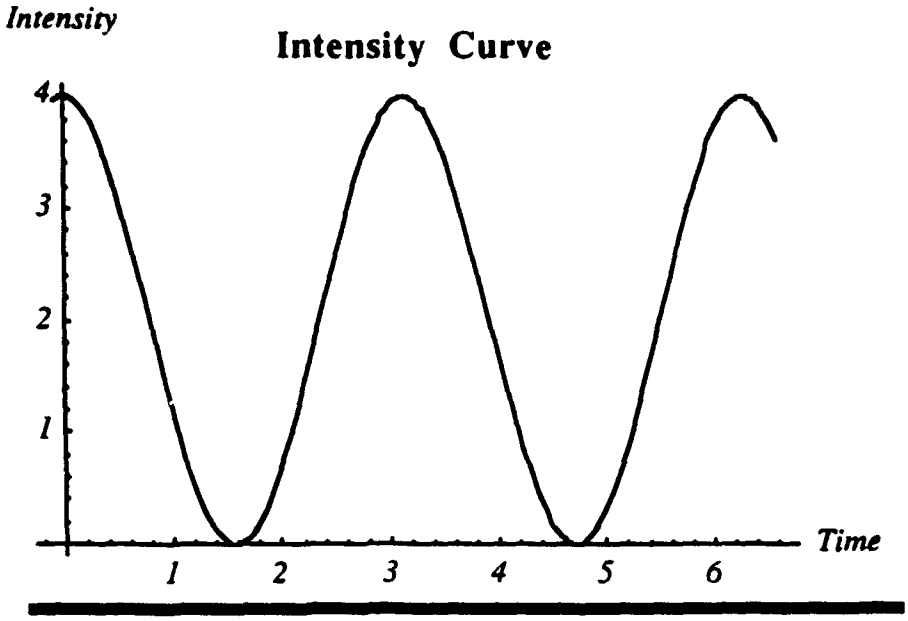

Figure 2-5 "Mode Beating Non Pulsed"

This behavior is readily seen in a Q-switched laser [15] with two longitudinal modes as shown in Figure 2-5.

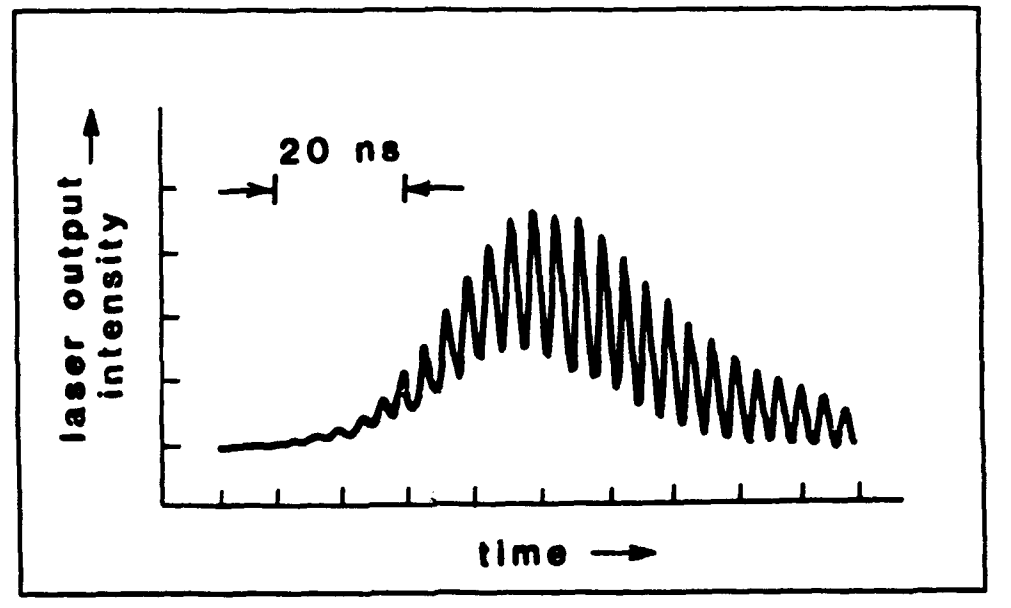

Figure 2-6 "Mode Beating in a Q-Switched Laser"

When only two modes are present, this type of "mode-locked" pulse is called mode-

beating. The phase terms in equation 2.4-3 are not relevant to the shape of the intensity output in this case as the mode-beating pulse is always "mode-locked". When three or more modes are summed together, interesting features develop in the intensity output as the relative phase terms are brought into alignment. Mathematically, the same process as above can be repeated for N frequencies with axial frequency spacing of ω_{ax}. The electric field is [16]

$$E(t) = \sum_{n=0}^{N-1} e^{j(\omega_o + n\omega_{ax})t} = \frac{e^{jN\omega_{ax}t} - 1}{e^{j\omega_{ax}t} - 1} e^{j\omega_o t} \qquad [2.4\text{-}4]$$

And the output intensity is

$$I(t) = |E(t)|^2 = \frac{1 - \cos N\omega_{ax}t}{1 - \cos \omega_{ax}t} = \frac{\sin^2 N\omega_{ax}t/2}{\sin^2 \omega_{ax}t/2} \qquad [2.4\text{-}5]$$

The mathematical effect of this series and its ability to create "mode-locked" pulses is illustrated quite well for the cases of N = 3, 4, 5, 6, and equal amplitude waves. In each case, the peak intensity of the summed wave is N^2 times the peak of an individual frequency. As can be seen in the Figure 2-7, it takes very few summed waves, if brought into a constant phase relationship, to produce a series of short intense pulses. The pulses will be separated by a time spacing of T if each wave repeats itself in a periodic interval of $t = t_0 + nT$ for n, an integer [17].

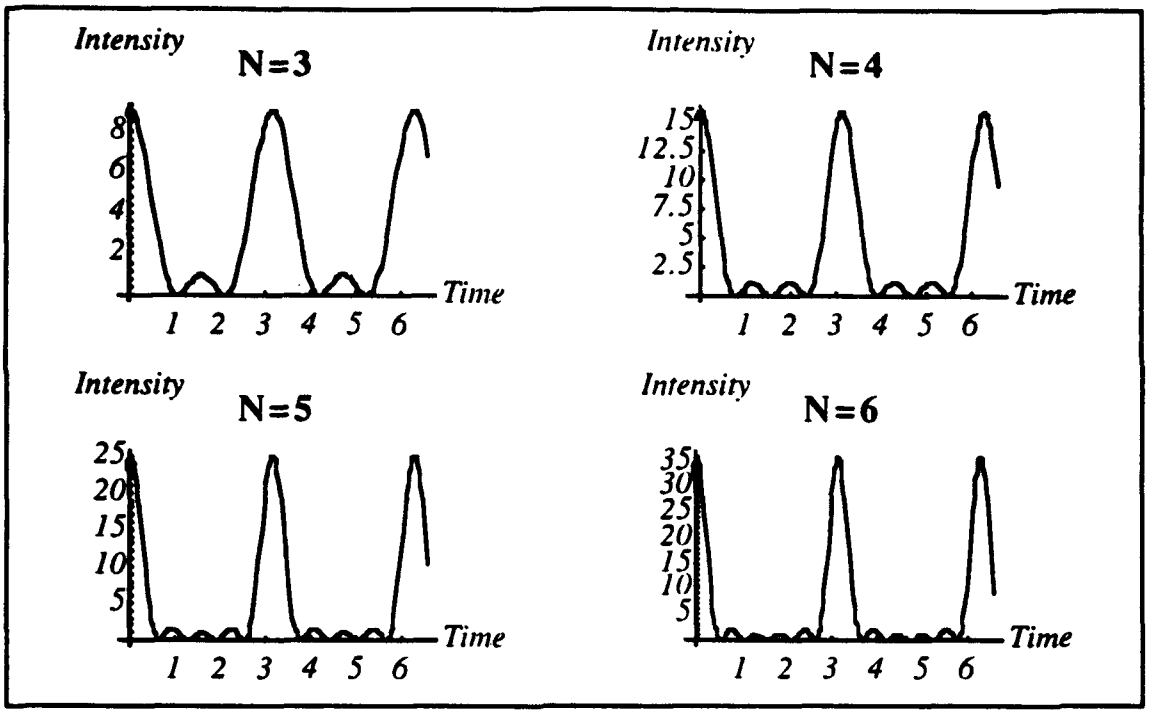

Figure 2-7 "Multiple Frequency Summing"

2.5 Loss Modulation

The term Loss Modulation provides a starting point to describe what happens when a "Mode Locker" is placed inside a laser cavity to create ultra-short pulses through AM (amplitude) modulation. A Loss Modulation device, as the name implies, provides a periodic source of transmission within a cavity experiencing buildup via stimulated emission. The modulator is driven at a frequency which corresponds to the round trip time of light within the cavity. The diffractive loss provided by the modulator insures the needed constant phase relationship between frequencies (separated by the c/2l cavity frequency) building within the laser cavity. The number of in-phase frequencies that will survive depends ultimately upon the amplification bandwidth that the laser gain medium can support. In addition, this frequency summing process differs significantly for gain media whose broadening mechanism is homogeneous or inhomogeneous. Broadening types will be discussed in more detail shortly.

Modulator Types

Various methods have evolved to produce periodic loss mechanisms capable of being inserted into an optical cavity. All modulators produce a periodic change in the index of refraction (n) along a zone of interaction within the material that the internal laser field also intersects. Electro-optic Modulators (EOM's) use a varying electric field applied to a material which then induces a periodic change of the index of refraction of the material. The Acousto-optic Modulator (AOM) also provides the same variation of index of refraction but uses instead, acoustic standing waves generated by a piezoelectric device attached to a material which is sensitive to sound waves. Both devices provide an equal forum for discussion of the theory of loss modulation, but, for the purposes of this paper, I will focus on the AOM and its role in AM modulation.

Historical Development

The origins of the theory of acousto-optics can be traced to the work of Leon Brillouin, who in 1921 published his paper on the scattering of light by thermal acoustic agitation in liquids [18]. Brillouin's paper investigated the variation of index of refraction of a material to acoustic waves. The velocity of sound in the media being investigated were much smaller than that of the light so that Brillouin assumed it was essentially standing still. He then applied the Bragg condition

$$\sin(\phi_B) = p(\lambda/n\Lambda) \qquad [2.5\text{-}1]$$

where ϕ_B is the Bragg angle of incidence of the light beam, p is an integer, λ is the wavelength of the light, n is the index of refraction, and Λ is wavelength of the sound, to

theorize that incoming light is either Doppler frequency upshifted (p = 1) or frequency downshifted (p = -1) by the sinusoidal variation of the index of refraction. Figure 2-8 [19] depicts the setup well.

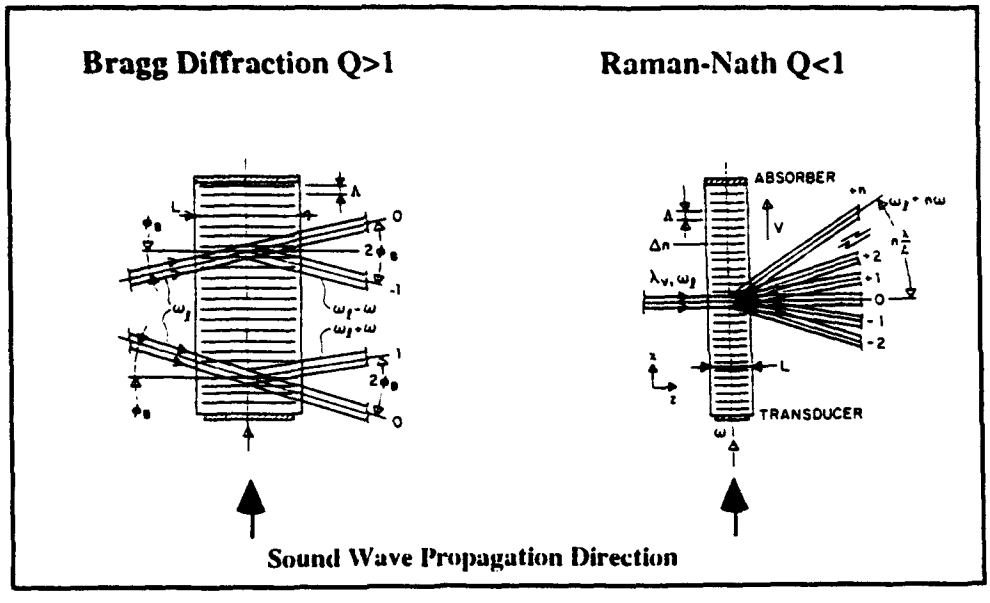

Figure 2-8a "Bragg Regime"

Figure 2-8b "Raman-Nath Regime"

Follow on experiments to Brillouin's work by Debye and Sears and Lucas and Biquard discovered a disturbing result that light incident upon the AO material was scattered into multiple orders of diffraction instead of the predicted two [20][21]. See Figure 2-8b [22] Raman-Nath. Debeye and Sears correctly assessed the problem as a limited zone of interaction within the material and derived the criteria under which the Bragg Condition could be met. The condition, in the original paper, was that L/Λ (L=interaction length and Λ=acoustic wavelength) is large compared to Λ/λ. This has since evolved into today's commonly used relation of [23]

$$Q = 2\pi \times \left(\lambda L / n\Lambda^2 \right) \qquad [2.5\text{-}2]$$

where Q is the quality factor and $\lambda L/n\Lambda^2$ is the Debye-Sears ratio. The explanation for the multiple order diffraction pattern and hence a more complete understanding of acousto-optic phenomenon came with a series of papers by Chandrasekhara Raman and N.S. Nagendra Nath [24]. From 1935 to 1936, Raman and Nath derived exact relations between multiple diffracted orders (see Figure 2-8b "Raman-Nath Regime") via a coupled-mode analysis.

Modulator Basics

The result of the historical development is that loss modulators are generally operated in one of two regions: the Bragg regime or the Raman-Nath regime. The location of each regime is determined by the Debeye and Sears relation [2.5-2] where

Raman-Nath Regime $Q < 1$

Bragg Regime $Q > 1$

Typical acoustic frequencies in the Raman-Nath regime are 10 MHz or lower [25]. As acoustic frequency is increased, the Raman-Nath multiple order diffraction disappears and the single orders of the Bragg regime prevail. The efficiency of an acousto-optic modulator to diffract light in the Bragg regime is [26]

$$\eta = \sin^2\left(\frac{\pi L(MI_a)^{1/2}}{\lambda\sqrt{2}\cos\phi_B}\right) \qquad [2.5\text{-}3]$$

where L = interaction length/sound column width

I_a = intensity of acoustic wave/acoustic drive power

M = figure of merit (FOM)

ϕ_B = Bragg angle (as defined previously)

The device figure of merit, M, is a nomenclature system first devised by Smith and Korpel [27]. The most commonly used value, M_2, is given by [28]

$M_2 = n^6p^2/\rho v^3$ where n is the index of refraction

p is the effective photoelastic constant

ρ is the density of the material

v is the velocity of sound in the medium

Other values of M have been developed and are M_1 which considers bandwidth [29] and M_3 which is independent of the optical beam dimensions [30]. Typical values are [31]

Material	Range of transmission [μm]	Wave-length [μm]	Density	Mode & propagation direction	v [10^5 cm/s]	Index of refraction	M_1 [10^{-7} cm s^2/g]	M_2 [10^{-13} cm s^3/g]	M_3 [10^{-13} cm s^2/g]
ADP	.13-1.7	.633	2.34	L(100)	6.15	1.58	16.0	2.78	2.62
Te	5-20	10.6	6.24	L(100)	2.20	4.80	10,200	4400	4640

Also, the modulation bandwidth of a typical device is in the Kilohertz range with the bandwidth defined by [32]

$$\text{Bandwidth} = 4\pi\frac{F_c}{Q_c} \qquad [2.5\text{-}4]$$

where Q_c is the value of Q [2.5-2] at the central frequency (F_c).

2.6 Amplitude (AM) Modulation

For amplitude modulation to occur, a loss modulator is inserted into a laser cavity experiencing buildup and modulated at the c/2l (longitudinal frequency spacing) or some multiple of it to allow the creation of circulating pulses of narrow width. Figure 2-9 [33] depicts how the modulator is operated in relationship to the longitudinal cavity mode spacing and the maximum transmission of the modulator where $2\Delta_m$ is the peak-to-peak modulation index or depth of modulation and $\omega_m = 2\pi \times (c/2l)$.

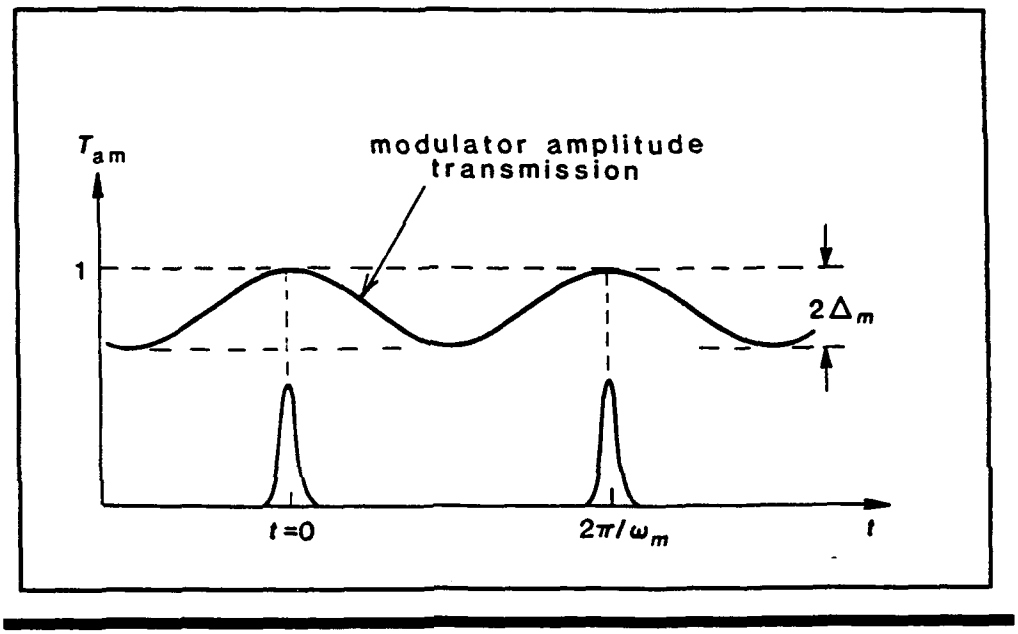

Figure 2-9 "Modulator Transmission Characteristics"

The mathematical analysis of AM modulation is carried out in a convenient manner using the circulating gaussian pulse analysis. The analysis is justified in its use of the gaussian pulse shape by the rapid convergence off an intracavity pulse to near gaussian form within a very few round trips, as seen in Figure 2-10 [34]. The way in which the gain is broadened dramatically changes the analysis. Homogenous broadening will be considered first and then the inhomogenous case.

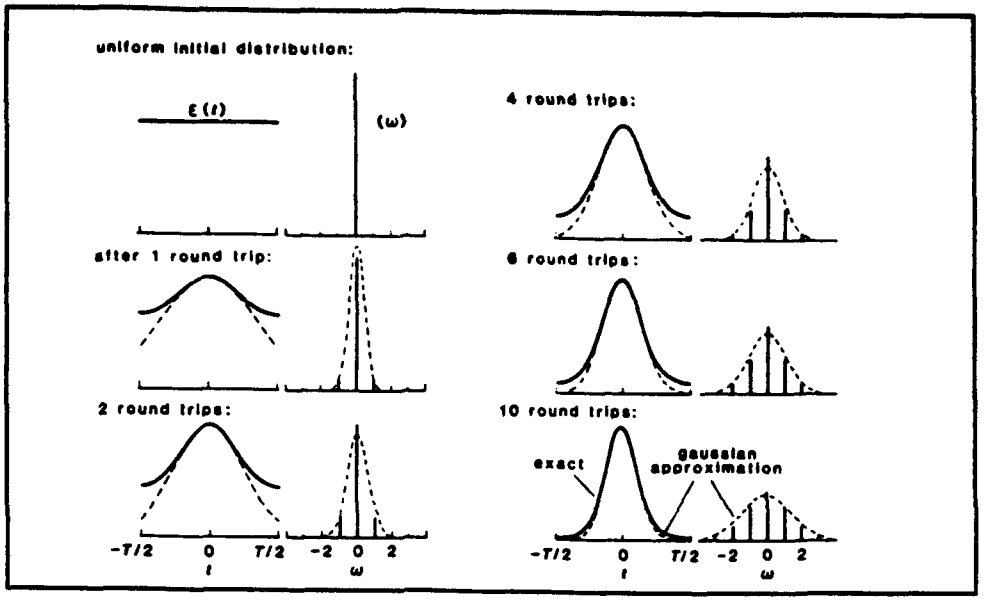

Figure 2-10 "Gaussian Pulse Convergence"

HOMOGENEOUSLY BROADENED GAIN

A circulating gaussian pulse analysis of a cavity without the mode locker installed yields the fractional change in the gaussian pulse parameter (before passage through the gain the parameter is unprimed and after is primed) as [35]

$$\Gamma' - \Gamma \approx -\frac{16\alpha_m p_m}{\Delta\omega_a^2}\Gamma^2 \qquad [2.6\text{-}1]$$

where Gaussian Complex Pulse Parameter is $\Gamma = \alpha - j\beta$

$E(t) = \exp\left[-\Gamma t^2 + j\omega_a t\right]$

$\tilde{E}(t) = \exp\left[-\frac{(\omega-\omega_a)^2}{4\Gamma}\right]$

$\alpha_m p_m$ = round trip gain coefficient

$\Delta\omega_a$ = atomic linewidth

The same analysis can be repeated with an AM modulator installed. The modulator

transmission function of such a device (see Figure 2-10) can be written as

$$\bar{t}_{am} = \exp[-\Delta_m(1-\cos\omega_m t)] \qquad [2.6\text{-}2]$$

where ω_m is an integer multiple of the axial frequency. Applying this equation and the condition that the pulse width is much shorter than the AM modulation period yields the fractional change in the gaussian parameter due to AM modulation [36]

$$\Gamma'' - \Gamma' \approx +\frac{\Delta_m \omega_m^2}{2} \qquad [2.6\text{-}3]$$

where the double primed parameter now indicates a change in the primed parameter after passage through the modulator. The pulse broadening (frequency narrowing) of [2.6-1] competes with the pulse narrowing (frequency broadening) of [2.6-3] and yields a steady state round trip solution of

$$\Gamma'' - \Gamma' \approx -\frac{16\alpha_m p_m}{\Delta\omega_a^2}\Gamma^2 + \frac{\Delta_m \omega_m^2}{2} \qquad [2.6\text{-}4]$$
$$= 0 \quad \text{for steady state mode locking}$$

In the steady state case, the gaussian parameter is [37]

$$\Gamma_{ss} = \left(\frac{\Delta_m}{\alpha_m p_m}\right)^{1/2} \frac{\omega_m \Delta\omega_a}{4\sqrt{2}} \qquad [2.6\text{-}5]$$

which leads to the useful expression for the steady state pulse width of a homogeneously

broadened gain medium of

$$\tau_{p,ss,h} \approx \left(\frac{\alpha_m p_m}{\Delta_m 2}\right)^{1/4} \left|\frac{1}{f_m \Delta f_a}\right|^{1/2} \qquad [2.6\text{-}6]$$

where f_m is the modulation frequency. From this it can be seen that the mode locked pulse width decreases with increasing modulation power and increasing gain bandwidth. This equation can also be written in another form as [38]

$$\tau_{p,ss,h} \approx \frac{0.5}{N_o^{1/2} f_m} \qquad [2.6\text{-}7]$$

where N is the number of modes that can fit under the FWHM of the gain bandwidth each separated by the cavity c/2l frequency.

INHOMOGENEOUSLY BROADENED GAIN

The analysis of inhomogeneously broadened gain, by contrast, is much easier due to the fact that frequency components sample the gain independently across the entire line width. In this situation, the mode locker device simply brings into phase the already oscillating modes as opposed to pushing energy into side band modes in the homogenous case. Therefore, in the inhomogenous case, the number of modes available is approximately the Doppler width divided by the axial mode spacing. Then, from Fourier Transform arguments, the pulse width is approximately [39]

$$\tau_p \approx \frac{.5}{\Delta f_d} \approx \frac{.5}{N_o \Delta f_m} \qquad [2.6\text{-}8]$$

where Δf_d = atomic linewidth

Δf_m = modulation frequency

N_o = number of modes present

3. EXPERIMENT

3.1 Apparatus Setup

The experimental apparatus for the longitudinally pumped photolytic I* laser is shown in Figure 3-1. A Questek Excimer Laser, using KrF, provides a pump source at 248 nm and is focused into the cell at the center of the gain medium. The dichroic mirror used to turn the beam into the cell is anti-reflection coated for 1.315 μ at 45^{o} while reflecting greater than 90% of the incident UV beam. Because of injection losses only, 66.5% of the energy of each excimer pulse is available to be absorbed by the gain medium. Excimer pulse energy averages about 220 $\pm 10mJ$ with a FWHM of 18-20 ns. Detection of the excimer pulse is via an FND-100Q fast detector. In most cases, this pulse serves as the trigger source for data collection. The exception occurs when detecting mode locked pulses. To achieve maximum real time sampling rates on the oscilloscope (1 GHz), only one source can be connected and hence becomes the trigger. Fast pulse detection of the laser IR pulse comes from an Opto-Electronics, 78 ps, ultra-fast detector displayed on a Tektronics 602A Oscilloscope. The combined detection speed limit of 1 ns is due almost exclusively to the preamp bandpass of 1 GHz on the plug in module of the oscilloscope. IR pulse energy detection is via a Laser Precision joule meter (Model RJP-735). The working gas in the cell is Iodotrifluoromethane, CF_3I. Purification of the gas, to remove any possible I_2, is accomplished by passing it through a copper mesh embedded within a glass cell line. All expended fuel is filtered through a cold trap and removed on a weekly basis. A standard Alcatel pump provides a nominal .030 Torr vacuum between gas fills.

The laser cavity used in this experiment has a stable hemispherical design with a 2 meter radius of curvature rear reflector and a flat output coupler of varying reflectivity. The Brewster windows on the gain cell were both CaF_2 and quartz. The quartz product used has an extremely low OH^- content (<5ppm). The latter, as will be seen, provided better UV transmission, eliminated the small water absorption line at 1.3 μm, and nearly tripled output energy. Finally, the mode locker and radio frequency (RF) synthesizer used were both products from the Intra-Action Corporation. The acoustic-modulator is a ML-503QWI model equipped with Brewster's windows, a 3 mm x 5 mm active aperture, water cooling, and an operating RF input frequency of 50 MHz for a standing wave modulation of c/2L at 100 MHz. The RF energy is provided by a model MLE-6B frequency synthesizer. This model can provide up to 10 watts of power in the range of 40 to 80 MHz with a resolution of 1 KHz. Although designed specifically for 1.06 μm light, this modulator and drive unit combination did provide a calculated 50% diffraction efficiency at 1.315 μm with an RF drive power of 1.94 Watts [40].

ALIGNMENT AND DETECTION PROCEDURES

The laser cell is aligned by standard methods using a HeNe laser. Fine tuning by optimizing energy output, however, is tedious due to the single shot nature of the experiment. Special attention to alignment of the IR energy meter is also needed to avoid pyrolytic effects on the metallic outer rim of the detector. Time based detection of the IR pulse requires optimization of the X-Y-Z positioning of the PD-20 and positioning of a Neutral Density (ND) filter which controls the 4% of the output beam taken to the detector. Detection of the UV pulse is relatively straightforward but is plagued by electromagnetic interference from the excimer laser thyratron. To reduce the noise in the UV pulse measurements, a Faraday Cage is placed around the detector and a piece of Plexiglas is placed under it to prevent possible ground loops with the table.

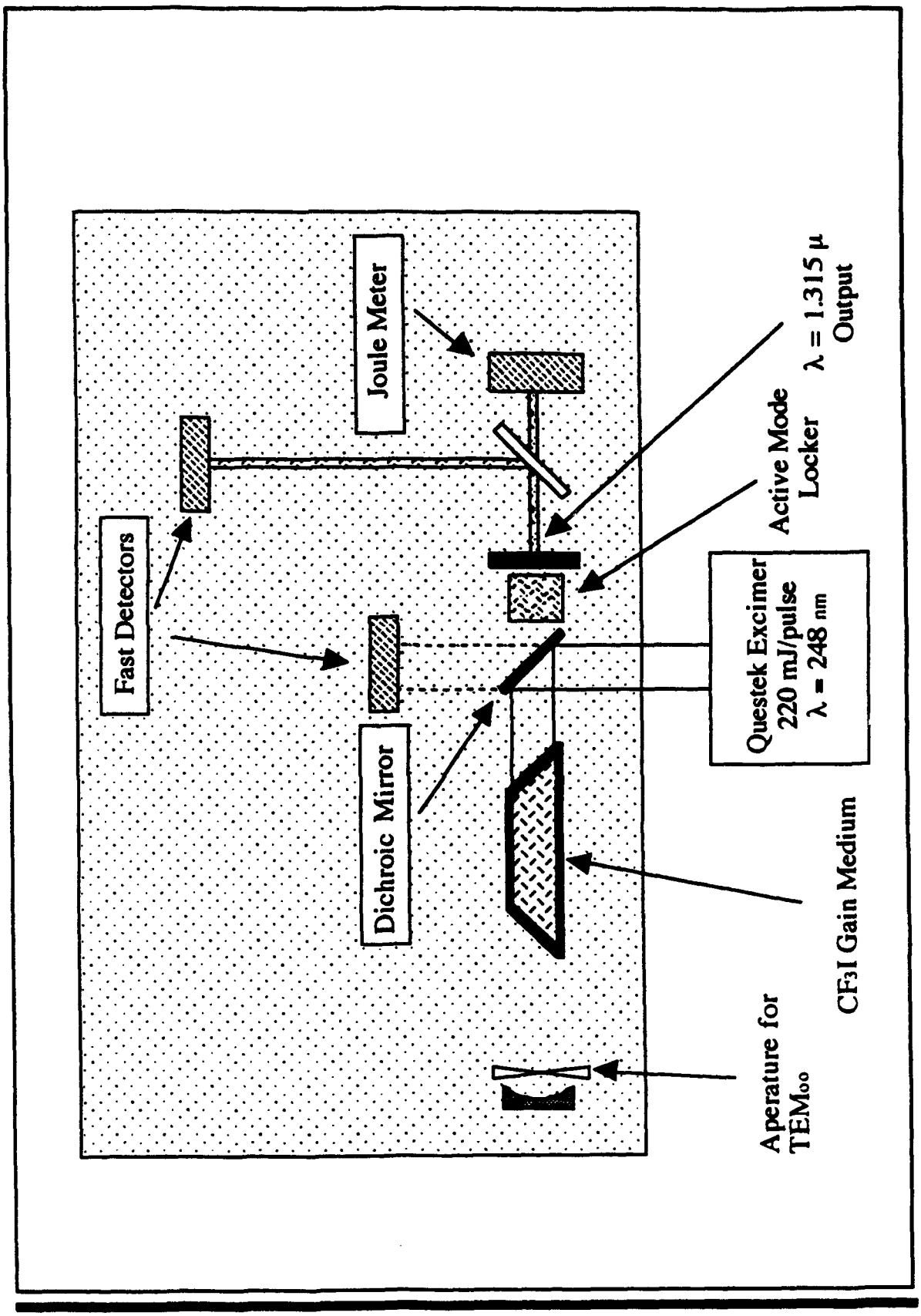

Figure 3-1 "Apparatus Setup"

FPI (Fabry-Perot Interferometer)

A 300 MHz FPI was used to sample the frequency spectrum of the IR diode probe output (see Figure 3-6). Of all detection devices used in this experiment, the very long 300 MHz FPI used as part of the probe setup, took the most time to align. The process of maximizing throughput while minimizing the line width is somewhat of a black art. By avoiding the expansion of the diode beam into the FPI, the time for alignment was reduced. The cost, however, was a reduction in the finesse of the device. See [3.3-1] and the discussion of finesse.

MODE LOCKER AND CAVITY SPACING

To obtain the correct angle, ϕ_B, for loss modulation in the Bragg regime, careful alignment of the AOM is critical. To accomplish this, the cavity is initially aligned with a HeNe laser and the AOM device in place. Once complete, the HeNe beam is modulated by the mode-locker operating with full power. The diffraction pattern, when viewed at the opposite end of the cell, can be adjusted to closely resemble Figure 3-2 by rotation of the Bragg angle

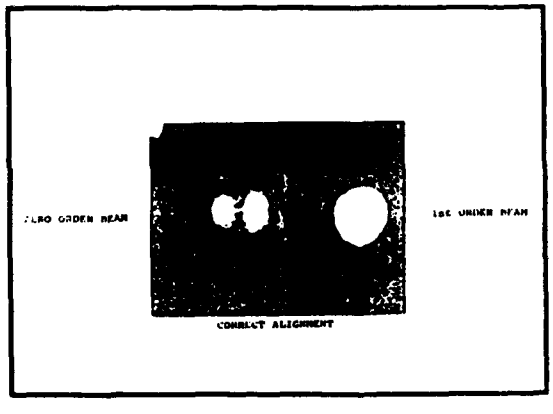

Figure 3-2 "Bragg Spot Pattern"

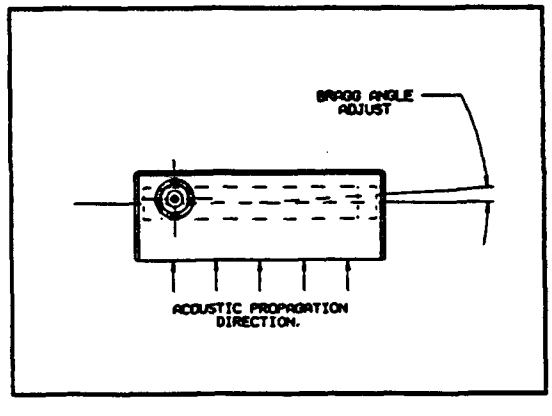

Figure 3-3 "AOM Rotation Axis"

about the axis listed in Figure 3-3 [41]. Although close to a good alignment at this stage, fine tuning of the angle is improved while the laser is operating at its 1.315 μm output wavelength. During this time, the cavity length must be very close to the correct length that corresponds to the axial frequency of (c/2L) or 99.992 MHz. The next step in alignment involves flowing the CF_3I to allow for a 2-3 Hz operation for a short period of time. When in this mode, the cavity length is adjusted with a linear translation stage on the rear resonator while the final Bragg angle adjustment is made. TEM_{oo} is selected by adjusting an intracavity iris while viewing the FFT of the output pulse. The transverse mode spacing of a resonator is given by [42]

$$\Delta f_{\Delta mnq} = \left(\cos^{-1}\sqrt{g_1 g_2}\right)\frac{c}{2\pi nL} \qquad [3.1\text{-}1]$$

where $g_i = 1 - \frac{L}{R_i}$

n = index of refraction

L = cavity length

c = speed of light

For the cavity length of 1.44 m, g_2=2 m, $g_1 = \infty$, the transverse mode spacing is approximately 33.6 MHz. All transverse higher order modes of this spacing decay below threshold as the iris is adjusted.

3.2 I* Laser Characteristics

To establish reliable measurements of this laser system, a constant knowledge of the pump energy and how much is deposited into the working gas is needed. At the start of the design process, a second dichroic mirror was not placed within the cavity to couple the

UV pump energy out of the laser for measurement. Instead, careful measurements were made of the absorption of pump energy by CF_3I at the various pressures to predict the absorption that would occur. A stochastic knowledge of the UV pump energy and its shot to shot deviation was made prior to each test. Data was taken only within 15 minutes of the measurement of mean pump energy. This short data time ensured that the excimer pump energy did not decay an appreciable amount. Figure 3-4 shows that data (as a percentage of mean shot-to-shot pulse energy) with an interpolation curve (spline fit with slopes not matched) between points. Keep in mind that each data point is a mean of 5 absorption values with a standard deviation that falls within the thick interpolation line. In addition, the decay of absorption for each fill of CF_3I was monitored for 5 additional shots of UV light. If the decay pattern did not show a consistent decrease in absorption of UV during the 5 shots (this situation is most likely a large error combination of the UV detector and UV pulse energies) then the data point was rejected and a new one taken.

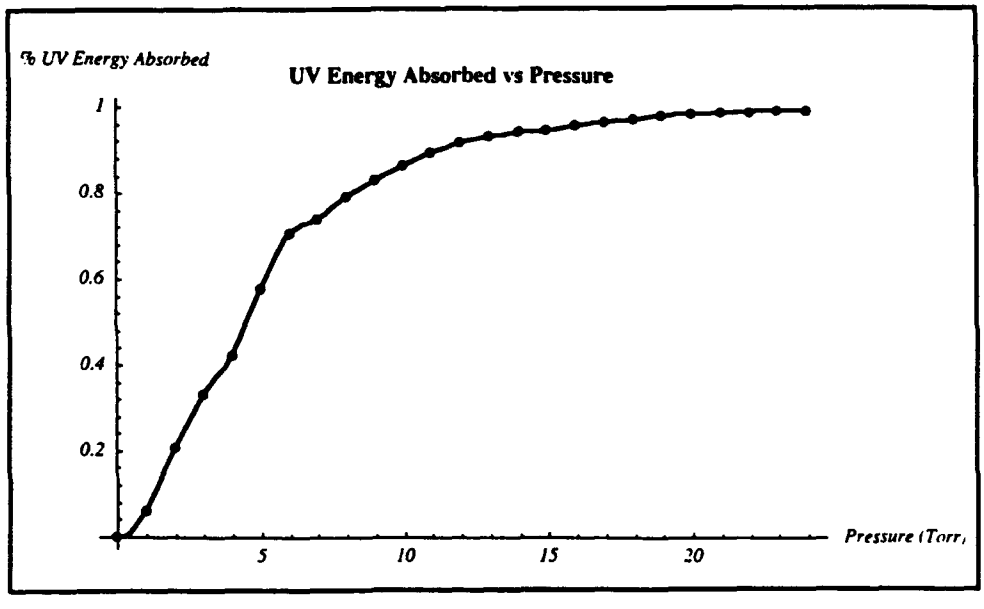

Figure 3-4 "Beer's Law Absorption for UV Pump Energy"

With these data, in the form of an interpolation curve, values of energy absorbed can be

inferred with reasonable assurance. To find the amount of UV light absorbed for a given shot, the mean UV energy is measured and multiplied by the 66.5% (measured percentage of energy available to the cell) and then multiplied again by the interpolation curve at the appropriate value of CF_3I pressure.

With the setup as described, the following data were taken prior to mode locking and will be discussed in Section 4:

Energy versus Pressure Curves

Power versus Transmission Curves

Cavity Buildup Time versus Pressure

Cavity Buildup Time versus Cavity Length

Mode Beating Profiles

Small Signal Gain versus Pressure

3.3 Small Signal Gain Measurement

DIODE PROBE DEVICE

To measure the gain in the cell after the gas has been excited by the UV pump, a narrow source of 1.31μm light from a solid state diode is used. This source of IR light has a narrow bandwidth compared to that of the gain medium, and its central frequency coincides with that of the hyperfine 3-4 transition. Figure 3-5 shows the diode probe setup. To provide a narrow source from a solid state 1.31μ diode device, a process of feedback and filtering is employed. Filtering is done by sending the multi-mode output of the diode through a 1 meter McPherson Monochrometer. The monochrometer uses a 1200 line/mm grating blazed at 1.2 μm with the entrance and exit slits wide open. This configuration allows a slit function that can pass most of the energy from a chosen

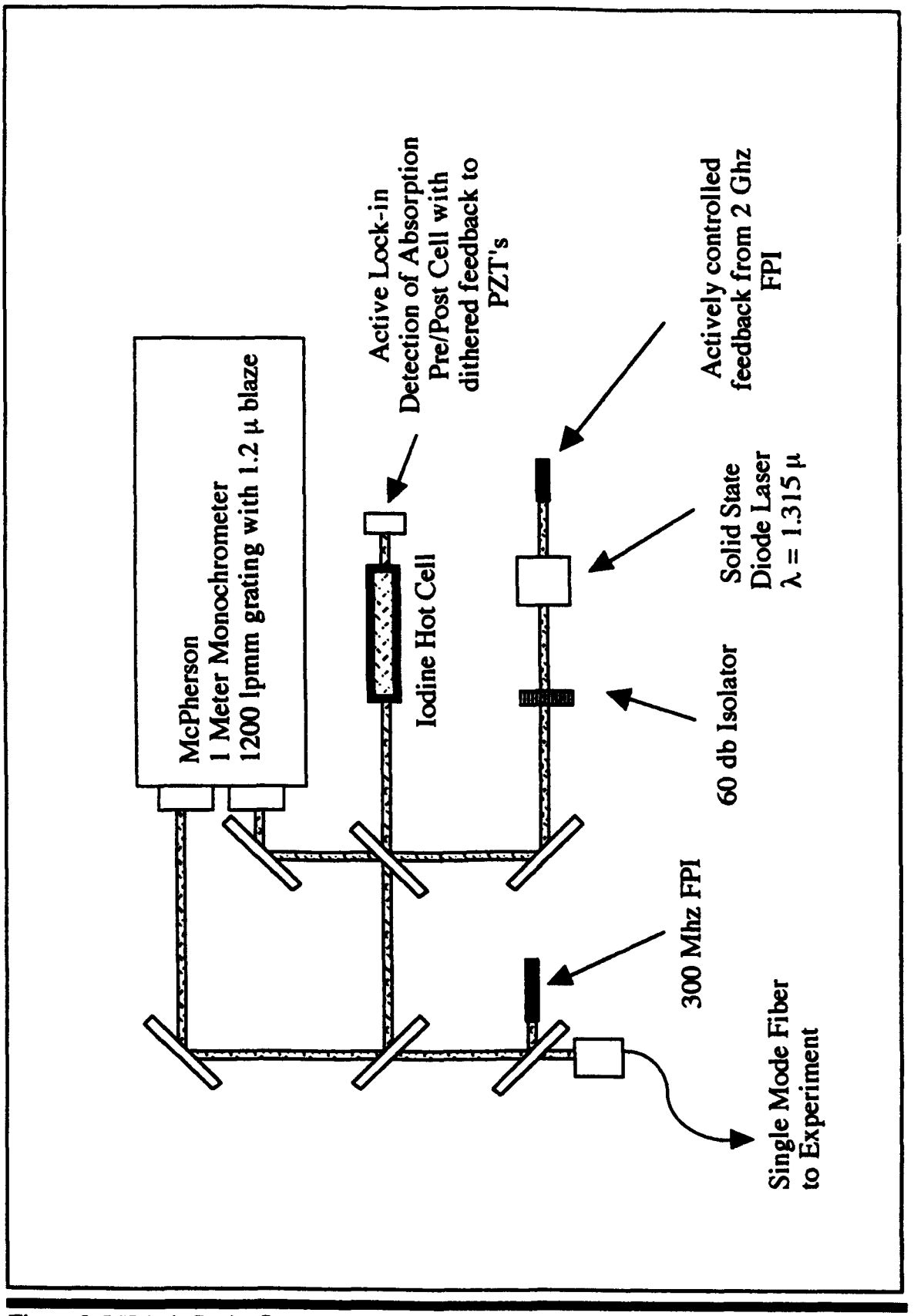

Figure 3-5 "Diode Probe Setup"

longitudinal axial mode while eliminating all others. The feedback provided from a 2.5 GHz Fabry Perot with piezoelectric positioning narrows the axial mode to be used while still preserving most of its output energy. To ensure that the resultant probe signal is precisely centered on the desired hyperfine 3-4 transition, it is sent into an iodine hot cell. The cell is kept at 630 °C to ensure the disassociation of I_2 into I. The probe signal is compared pre and post cell while scanning it with a ramped current source. In this manner, the absorption dips which correspond to the area of interest, can be found. The scan below, Figure 3-6, is centered on the area of the 3-4, 3-3, and 3-2 hyperfine transitions.

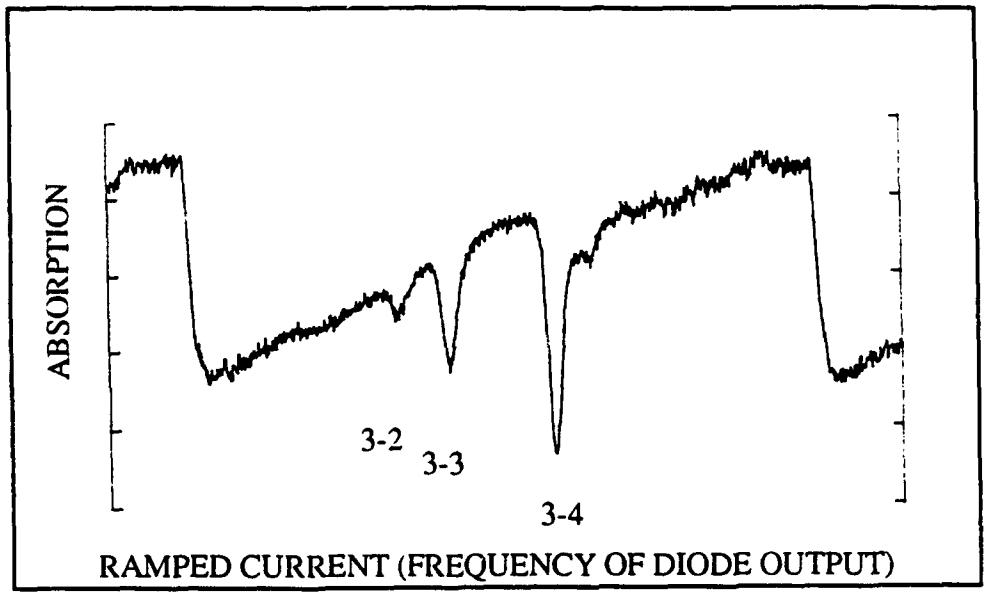

Figure 3-6 "3-4, 3-3, 3-2, Hyperfine Scan"

Selection of one of these absorption peaks is straightforward once the area is found. It is of considerable importance to note here that the entire hyperfine structure could not be scanned in a stable manner with current tuning alone. The particular diode used for this experiment could not reliably reach the hyperfine 2-3, 2-2, 2-1, transitions near threshold current, even with the use of both temperature and current tuning. In fact, it would only be through a combination of luck and extremely precise factory specifications that would produce a

diode whose output is centered between the 3 and 2 hyperfine transition levels so that it could be scanned across its linear current regime at a low non-multimode temperature and reach both hyperfine areas.

Once the final signal is prepared, its bandwidth is checked on a 300 MHz Free Spectral Range (FSR) Scanning Fabry Perot Interferometer. The oscilloscope trace below, Figure 3-7, is typical.

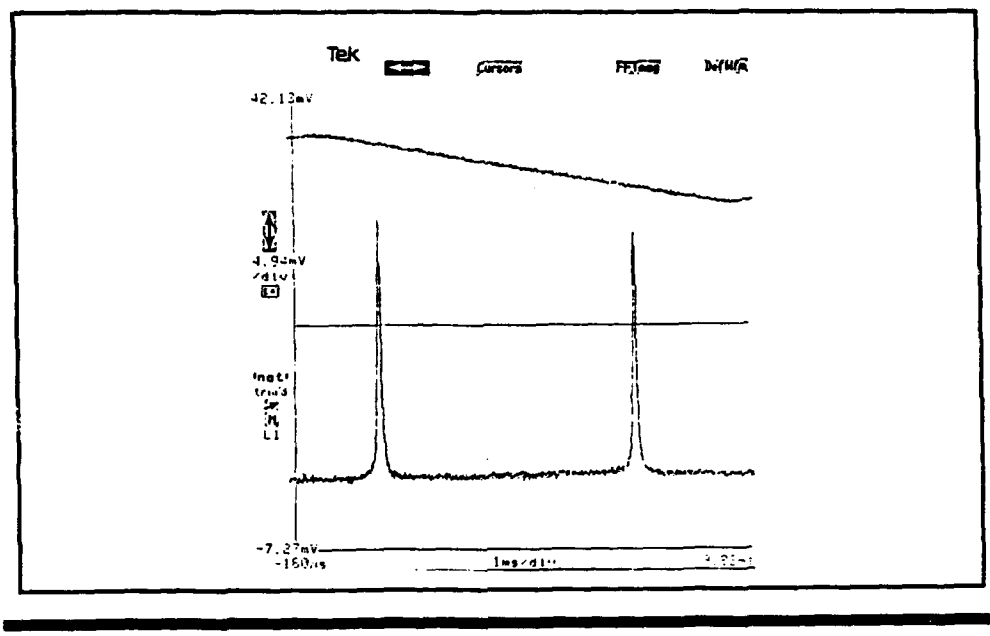

Figure 3-7 "5 MHz Probe Scan"

The finesse of a Fabry Perot device is given by

$$F = \frac{\Delta \upsilon}{\Delta \upsilon_{1/2}} \qquad [3.3\text{-}1]$$

where $\Delta\upsilon$ is the FSR and $\Delta\upsilon_{1/2}$ is the bandwidth of a transmission maximum, defined as the full width at half maximum. The finesse of the device used is near 150, but the results in the actual measurement gave a value 60. The difference in the two values can be attributed to the alignment process where the input beam was not expanded to fill the entire

mirror aperture. The measured value, however, is acceptable because the width of the probe signal is less than or equal to 5 MHz. Therefore, in relationship to the gain bandwidth (>250 MHz), the probe signal is much more narrow and the need to perform a deconvolution of the measured signal to get the true gain is negated.

GAIN MEASUREMENT SETUP

The output of the probe setup is sent via a single mode fiber to the experiment. To reduce unwanted spontaneous emission from the cell into the measurement, a double pass system is used as shown in Figure 3-8 where the fiber input comes from Figure 3-6.

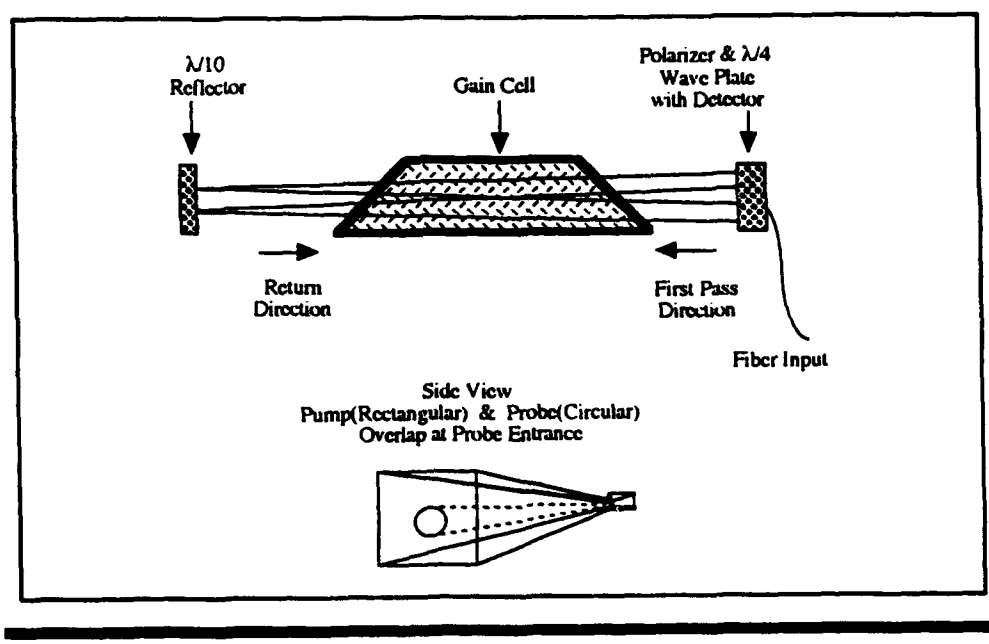

Figure 3-8 # "Pump and Probe Overlap"

The fiber output is sent through a combination linear polarizer and quarter wave plate before traveling down and back through the cell. With fiber collimating optics, the signal was focused at the center of the cell during the first pass to match the tapered profile of the pump beam. Upon reflection, the beam diameter was not controlled and, therefore, a small

probed volume, upon return, is not excited by the pump. As can be seen by the figure, the excimer pump beam is rectangular with dimensions of 12.7 mm x 19.1 mm at entrance into the gain cell. A variable X-Y positioning device was built allowing the entire fiber/detector combination to be positioned at the optimum gain location. The final output is monitored by a Judson J16D germanium IR detector. For all measurements the Judson was biased in the fast detection mode and was uncooled. With the setup as listed above, the gain was measured in two different ways.

DIRECT MEASUREMENT

The first measurement was via direct detection of the signal with and without amplification. To accomplish this goal, the probe signal with (I) and without (I_o) amplification must be known. Once I and I_o are known, a Beer-Lambert absorption can be assumed to obtain the value of small signal gain per unit length. The formula used is

$$\frac{I}{I_o} = \frac{V_{Baseline} + V_{Gain}}{V_{Baseline}} = e^{\alpha_o L_g} \qquad [3.3\text{-}2]$$

where L_g is the total gain length probed, α_o is the gain per unit length, $V_{Baseline}$ is the baseline voltage, and V_{Gain} is the voltage with gain. It is of importance to note the detriment in using a Beer-Lambert absorption to distribute gain across a medium whose absorption profile is most probably not an exponential one. The problem here is that due to optics limitations, the UV pump for the gain cell had to be focused into the middle of the cell. This type of focusing creates a greater region of gain in the middle of the cell than would be expected from a standard pump beam where gain would exponentially decrease from the beginning to the end of the cell.

3.4 Mode-Locking

With the I* laser fully characterized, the mode-locking experiments were started. After the alignment procedures (see section 3.1). The following data was taken

Pulse Width versus Pressure (CaF_2 and Low OH^- Windows)

Pulse Width versus Modulation Intensity (CaF_2 and Low OH^- Windows)

Results and discussion are located in section 4.4.

3.5 Multi-Pulse Effects

The last experiments to be accomplished were observations of the multi-pulse effect at low pressures. The laser setup was changed, after exploration with the computer model, so that no intracavity elements (except the dichroic turning mirror) were present and the shortest possible cavity length obtained. Studies of the pulse output versus pressure were made with considerable damage to cavity resonator optics at the lowest pressures due to the still focused UV pump beam. All results and theoretical conjecture of the double pulse observations, though extremely interesting, do not bear a direct impact on completing the mode locking goals of this experiment. Therefore, this information will be placed in Section 6 under future experiments.

4. RESULTS AND DISCUSSION

4.1 I* LASER CHARACTERISTICS

With the setup described in Section 3, data were taken on energy versus reflectivity /transmission for the longitudinal laser cell. The following six graphs were then selected (Figure 4-1 & 4-2). The cavity length is 1.44 m, the gain length is 22.4 cm, and the cavity configuration is hemispherical (2 m curvature). The optimum energy output occurs at a pressure near 20 Torr with an output coupler of 70% reflectivity. Each curve of energy versus pressure of CF_3I exhibits expected rollover behavior at high pressures. The high gain of this laser is exhibited by the last graph in Figure 4-1 which shows significant energy output even with a piece of glass as the output coupler. The graphs of Figure 4-2 show a greater variation in the data points due to the need to realign the laser cavity and detectors for a change in output coupler.

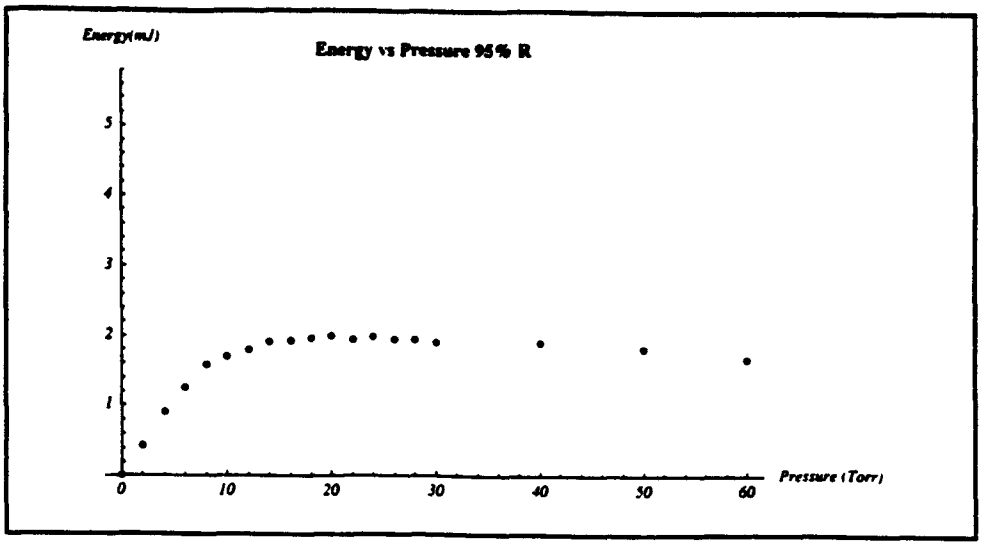

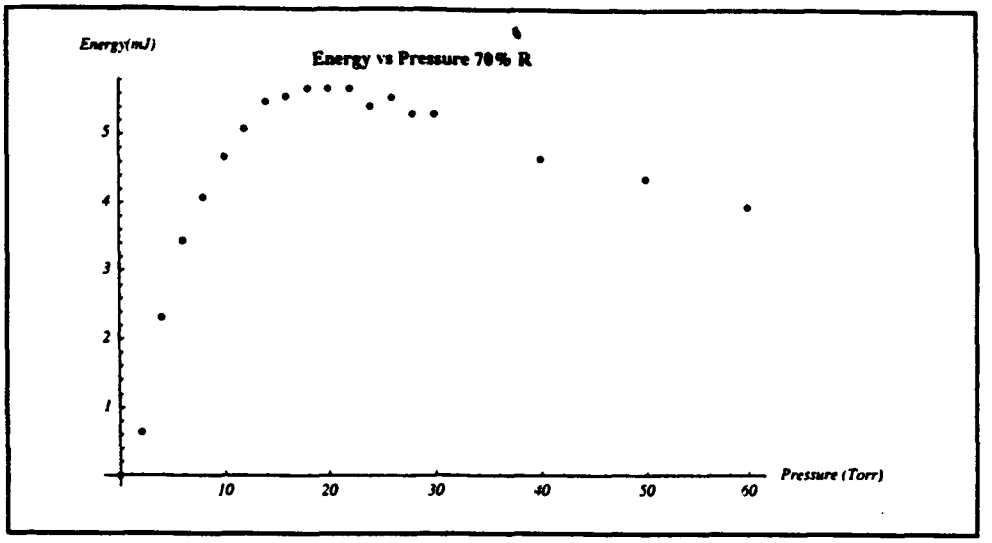

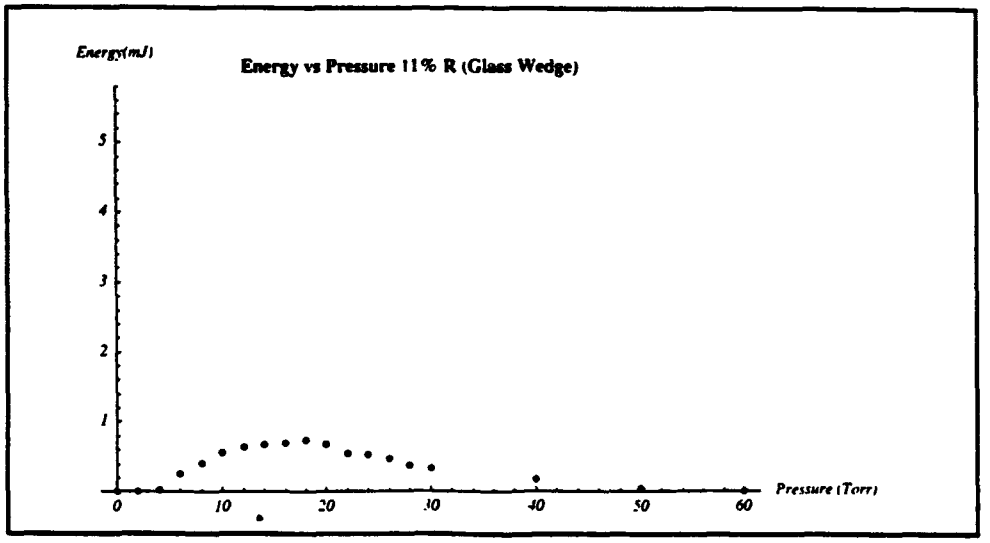

Figure 4-1 "Energy vs Pressure at R = 11,70,95"

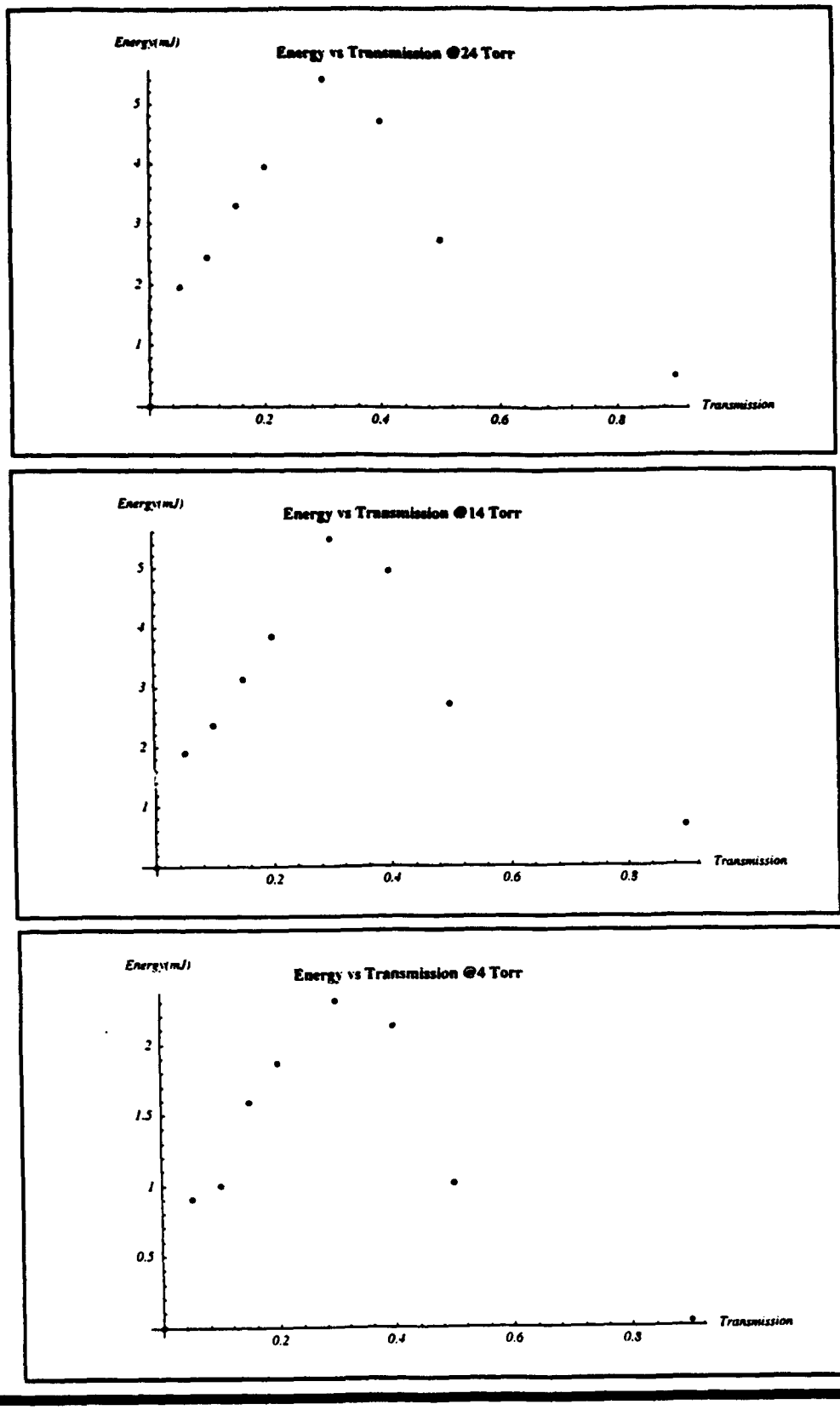

Figure 4-2 "Energy vs Transmission @ 4, 14, 24 Torr"

The following graph depicts power versus output coupler transmission under optimum conditions. The rigrod type curve fit is drawn to aid the eye only.

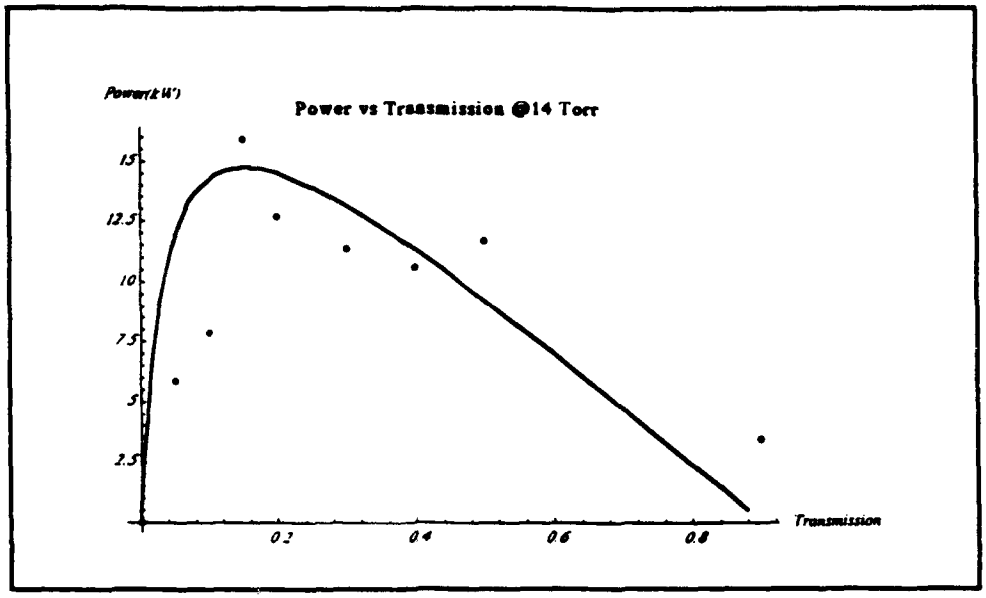

Figure 4-3 "Power vs Output Coupler Transmission @ 14 Torr"

The peak energy and power of 5.7 mJ and 15.5 kW of were recorded at 14 Torr with the 30% transmission output coupler. For this case, the average excimer UV energy was 238 mJ. 66.5% of this energy is available to the gas which at 14 Torr absorbs 92% (see Figure 3-5). In all, 144 mJ is absorbed by the CF_3I at 14 Torr. Each quanta of light absorbed at 248 nm produces an I* which can lase. Therefore, at most, 1.8 x 10^{20} I* atoms are produced during photolysis. If all of these I* atoms were to lase through stimulated emission, the output energy could be 18.13 mJ. This yields an extraction efficiency of

$$\eta_{eff} = \frac{\text{Measured Output Energy}}{\text{Theoretical Output Energy}} = \frac{5.7\ \text{mJ}}{18.13\ \text{mJ}} = 31\% \qquad [4.1\text{-}1]$$

The relative shape of the curves and their departure from a smoother look at the 50% transmission output coupler data point is most likely due to systemic reasons. First, the 50% output coupler was quite large in size (6") and required a temporary movement and

realignment of the energy and pulse shape detection system. Second, this set of data points was taken last and after a long (almost 3 hour) delay. The possibility of poor realignment and excimer output energy decay can account for the droop in the curves at 50% transmission.

ENERGY VS TRANSMISSION (DIFFERENT WINDOW MATERIALS)

It is of interest to note the impact of changing Brewster window material while keeping all other parameters fixed or as close to the previous measurements as possible. The specialized quartz material offered an improved transmission of UV light by 5% while essentially eliminating the water absorption line at 1.32 μm present in both CaF_2 or "normal" UV grade quartz. Energy extraction of the laser improved by nearly three times.

CAVITY BUILDUP TIME VS PRESSURE

The cavity buildup time is measured from the peak of the UV signal to the onset of a detectable rise in the IR signal with the math functions of the digital oscilloscope. The graph displays the results for the 14 Torr case at the optimum output coupler of 30% transmission. The graph also shows the expected dip in the cavity buildup time near the optimum energy output. The buildup time increases at the extremes of low and high pressure, as expected.

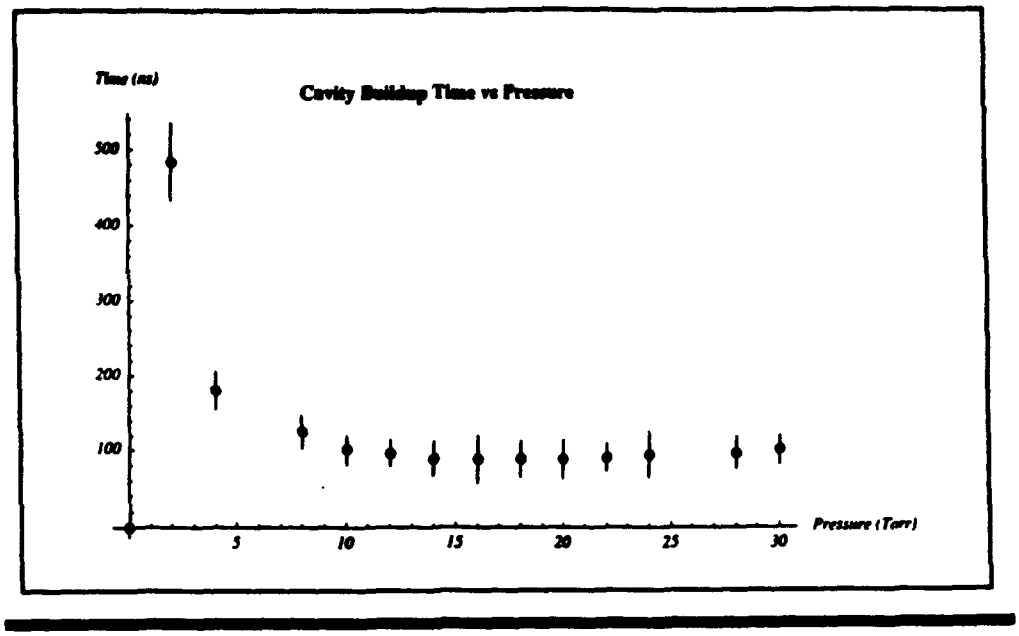

Figure 4-4 "Cavity Buildup Time vs Pressure"

The same procedures are employed to make the cavity buildup time versus cavity length measurements as per the previous graph. Figure 4-5 shows the results. At long cavity lengths a linear increase of buildup time with change of pressure results. Data below 1.2m could not be taken due to mirror damage, but cavity buildup time there would level off to minimum value.

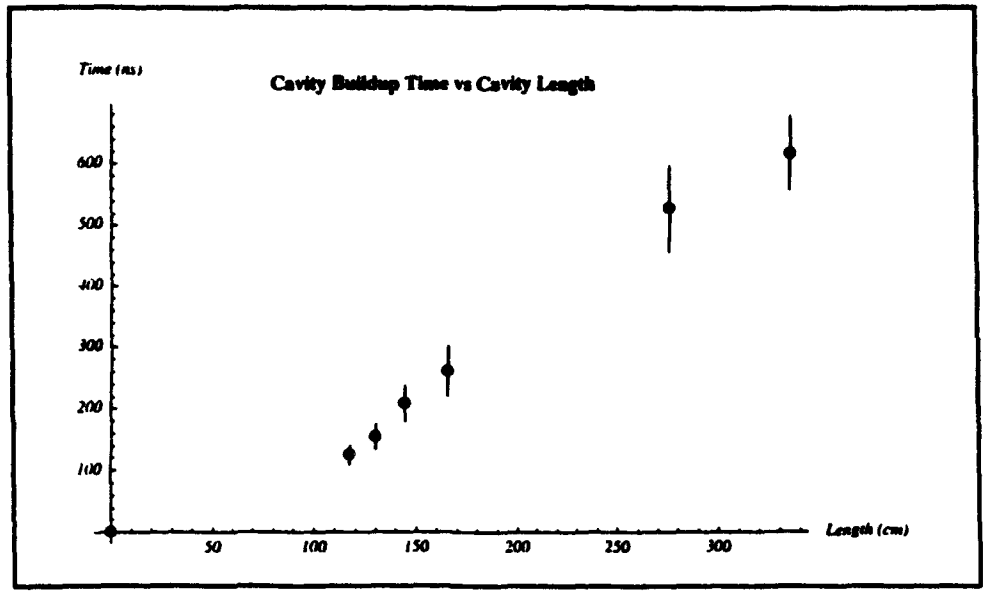

Figure 4-5 "Cavity Buildup Time vs Cavity Length @ 18 Torr"

MODE BEATING FOR TWO LONGITUDINAL MODES

Some time was spent examining the transverse and longitudinal structure of this laser just prior to mode locking (see "Alignment Procedures"). With the appropriate adjustment of the intracavity iris and selection of a very low pressure of CF_3I, the gain bandwidth can be made small enough to support only two modes. Classic mode beating (see Section 2.3) is the result. Figure 4-6, shows typical oscilloscope traces with associate FFT (Fast Fourier Transform) confirming the longitudinal mode spacing at a 100 MHz.

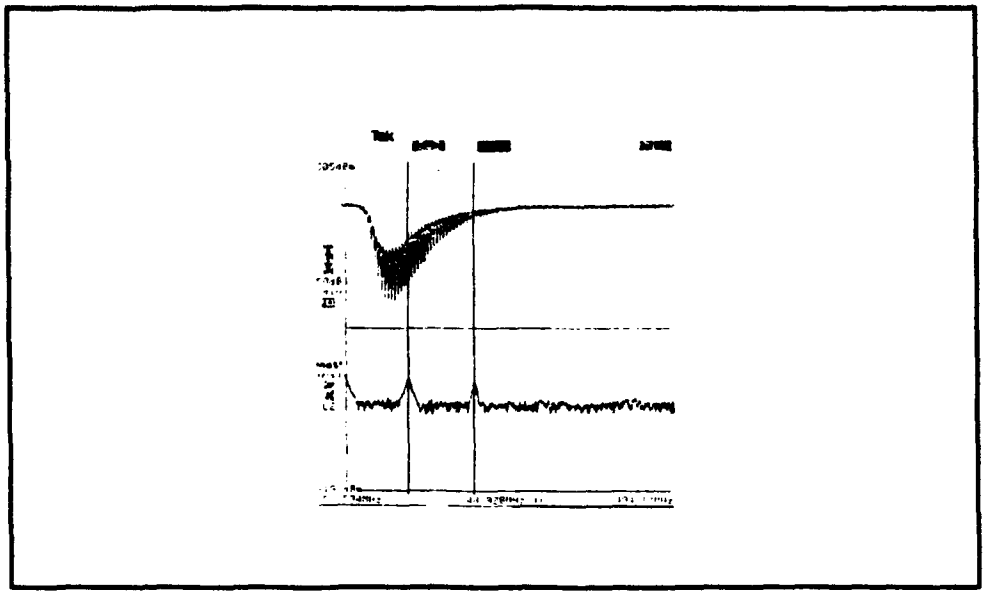

Figure 4-6 "Mode Beating @ 2 Torr with associate FFT"

4.2 GAIN MEASUREMENTS

DIRECT MEASUREMENTS

All measurements of gain versus pressure were time based in nature using the setup described in Section 3. A mechanical chopper was placed into the probe beam path and the AC component of the voltage signal was measured to get I_o. The baseline or I_o measurement was repeated for each value of pressure to insure consistency when faced with thermal or vibrational variations in the output intensity of the probe beam. The value of I is obtained from the addition of the AC component of the probe with and without gain. Peak small signal gain is then calculated from [3.3-2]. Fluorescence from the optical components due to the UV pump beam could not be completely filtered out. Even with a second dichroic mirror placed in front of the detector to dump the residual UV energy aside, fluorescence from the optical components could not be removed. To compensate for this in the final measurement, a time based trace of the effect was subtracted using

oscilloscope math functions. As before with the baseline measurements, a new trace of florescence was taken with no gas in the cell prior to each pressure reading. Figure 4-7 shows the process of removing fluorescence from a typical measurement.

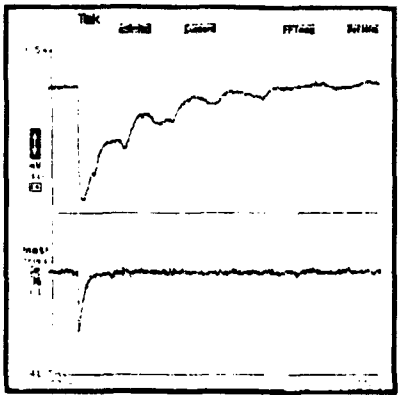

Signal with Gain Upper Plot
Flourescense Only Lower Plot

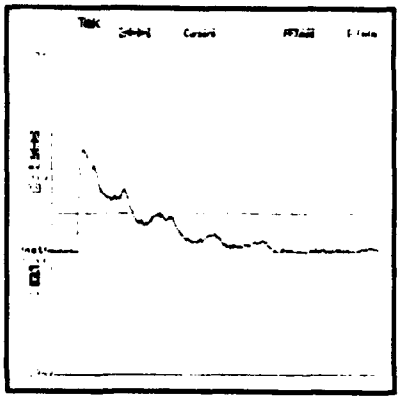

Final Signal for Use in Peak
Signal Gain Measurements

Figure 4-7 "Fluorescence Subtraction"

It is interesting to note the acoustic shock wave (changes in the index of refraction) overlaid on the gain measurement. The time required for one period of the wave (just after the peak gain) is the time needed for a radial shock wave to travel from the center of the gain cell, reflect off the walls, and return to the center at 298 °K. To complete the broader picture of gain versus pressure, the peak value of gain for each trace (as depicted in Figure 4-7) was used in the following graph.

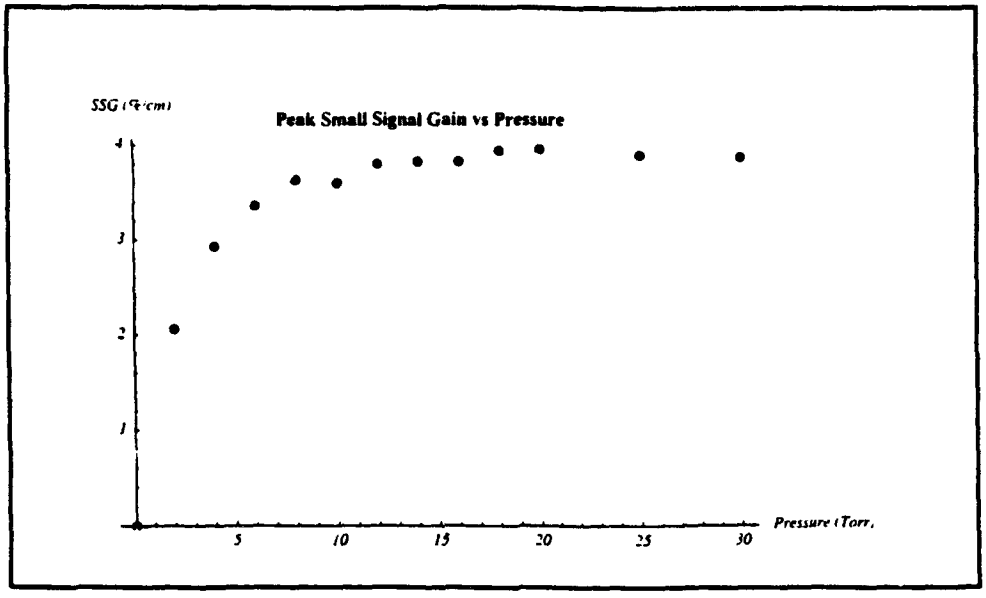

Figure 4-8 "Peak Small Signal Gain vs Pressure"

BACKUP TO DIRECT MEASUREMENTS

One method of checking the results of the direct gain measurement, is to calculate the amount of UV energy deposited within the cell and then to check to see if the volume probed by the diode laser is sufficient to account for the gain. This type of check, however, is subject to strong error influences. The variation in UV shot-to-shot pulse energy along with the inability to obtain an accurate probe beam diameter, makes this measurement only good enough to provide an upper and lower bound for the direct measurement.

First of all, the pulse-to-pulse average energy is measured. Secondly, the shape of the probe beam is measured at both entrance and exit to provide an accurate picture of the volume of excited iodine being probed. Figure 3-8 depicts the probe shape along with that of the pump beam. Once the pumped volume and the probed volume is known, the overlap can be computed to get the volume of I* that has been interrogated. This overlap is about 50%, but on the return trip of the probe beam through the pumped region, a significant area

of non-overlap occurs, hence the large error in this calculation.

Using the experimental evidence, discussed in section 2.1, that one photon of incoming UV light photolizes CF_3I into CF and I*, the value of gain can be obtained. The needed gain equations are

$$\gamma = \frac{A_{34}\lambda^2}{8\pi} g(\upsilon)\left[N_{upper} - \frac{g_{upper}}{g_{lower}} N_{lower} \right] \qquad [4.2\text{-}1]$$

where A_{34} = Einstein Coefficient for 3 - 4 Transtion
λ_{34} = Wavelength for 3 - 4 Transtion
N_{upper} = Population of Upper State which is Lasing
N_{lower} = Population of Lower State which is Lasing
$g(\upsilon)$ = Line Shape Function

This reduces to

$$\gamma = \sigma\left[7/12\, N_{upper} \right] \qquad [4.2\text{-}2]$$

where $\sigma = \frac{A_{34}\lambda^2}{8\pi} g(\upsilon)$

due to the assumption that during the photolysis event the population is deposited with statistical weighting into only the upper hyperfine levels where the population in F=3 is 7/12 's of the total I* produced. Figure 4-9 shows the combination of these calculations which provide upper and lower bounds when overlaid on Figure #4-8. Thus the direct measurements lie within the upper and lower bounds of gain that can be measured in the higher pressure regime (>10 Torr). However, direct measurements deviate from the bounds of possible gain at pressures less than 10 Torr. The reason for the deviation is possibly due to the optimization that was done to measure gain directly. The use of an X-Y positioning device to secure the highest peak gain measurements, ensures that lower

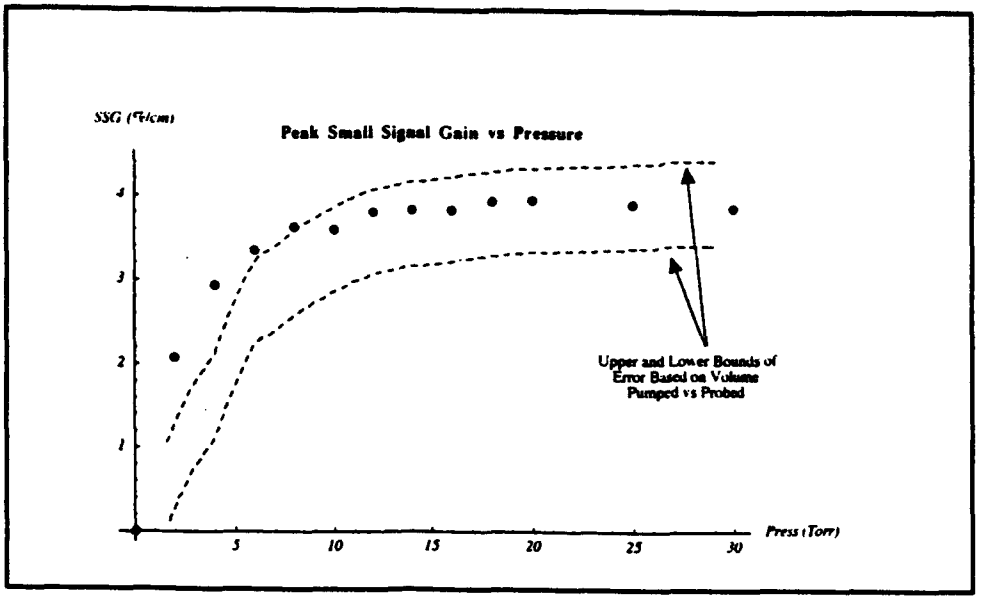

Figure 4-9 "Direct and Indirect Gain Measurements"

values would be obtained elsewhere. It is conceivable then, that if the average peak gain for various positioning of the probe device were plotted, the point values of gain in Figure 4-9 would fall between the error bounds throughout the range of pressures. This analysis is an indication of the non-exponential distribution of the gain within the cell due to focusing of the UV pump energy.

4.3 AM MODE LOCKING

The setup and alignment procedures for taking mode locked pulse data is listed in Section 3. As was stated previously, to achieve the maximum resolution of one nanosecond, the oscilloscope was reconfigured to trigger off only the IR source. Hence, the typical trace of Figure 4-10 does not include the UV pump pulse. The cutoff of the pulse train is due to the high threshold trigger required to avoid recording the electromagnetic noise from the excimer pump laser thyratron. At this point, a necessary step

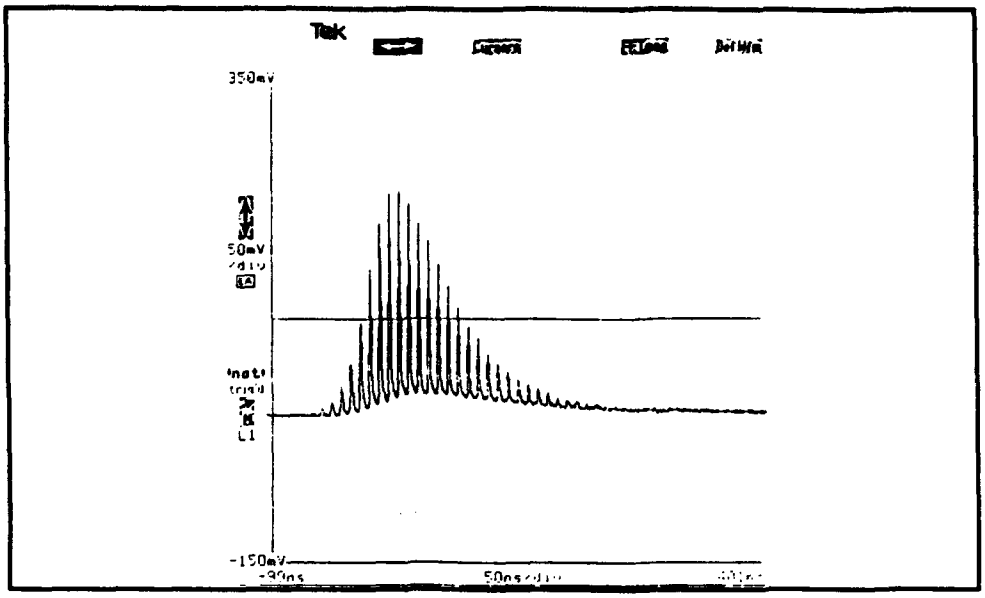

Figure 4-10 "Typical Mode Locked Pulse Train @ 4 Torr"

to confirm the experimental effects of the AOM modulation intensity on the pulse width is to create a plot of pulse width versus modulation intensity. Figure 4-11 represents the average pulse width within a pulse train for a given pressure of CF_3I.

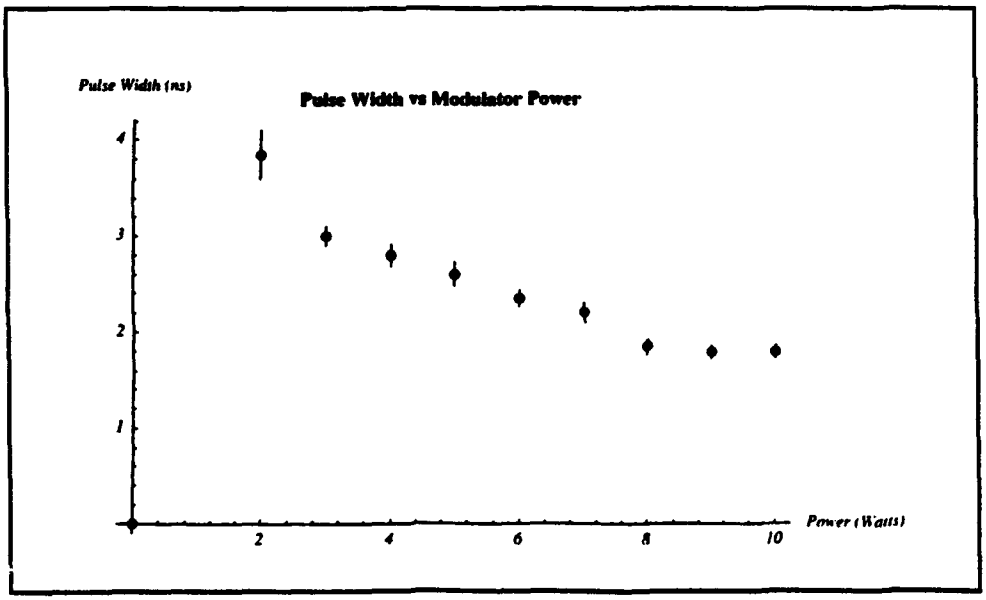

Figure 4-11 "Pulse Width vs Modulation Power @ 4 Torr"

This compares well to the theoretical dependence upon $\Delta_m^{-1/2}$ predicted by AM mode locking theory.

The following two figures, 4-12 and 4-13, represent the culmination of this mode locking experiment via two graphs of minimum pulse width versus pressure of CF_3I.

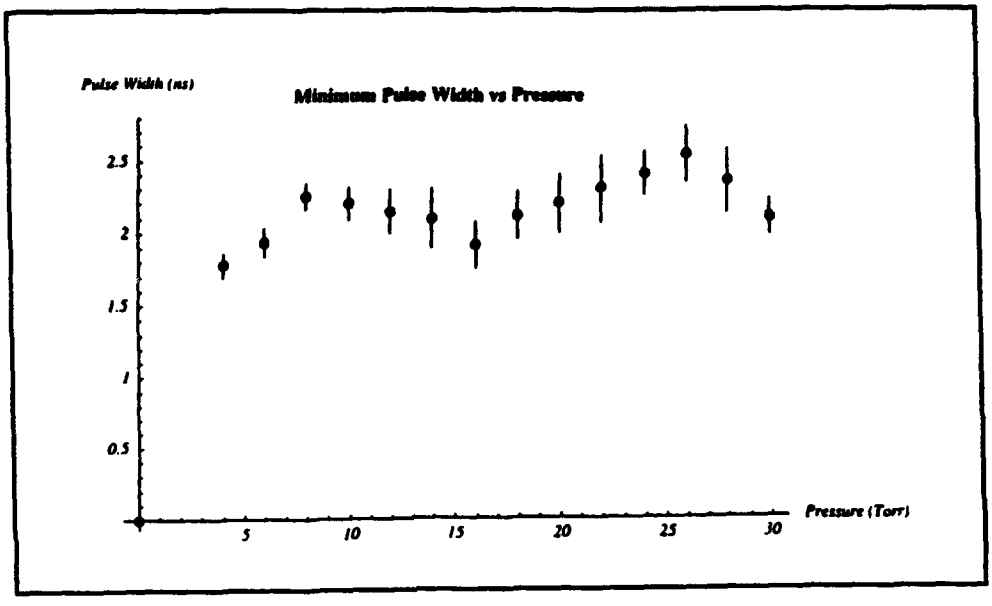

Figure 4-12 "Minimum Pulse Width vs Pressure CaF2 Windows"

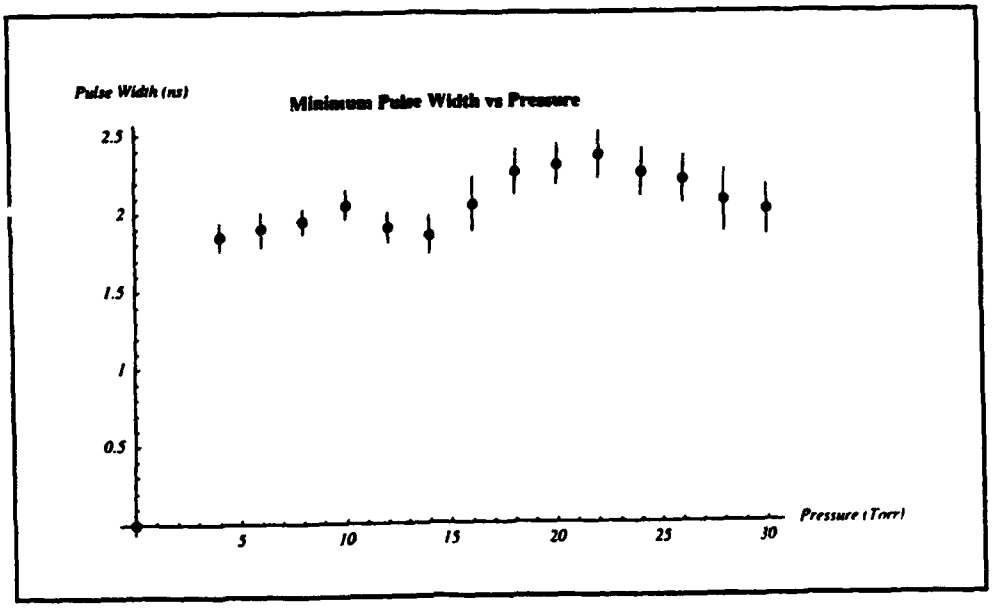

Figure 4-13 "Minimum Pulse Width vs Pressure for Quartz Windows"

The cavity parameters are: Cavity Length = 1.44 m, Gain Length = 22.4 cm, 30% transmissive output coupler, 2 m curvature rear mirror, and the modulation intensity at maximum. Close examination of these plots reveals some interesting results.

MINIMUM PULSE WIDTH

First of all, the smallest pulse width measured was with the CaF2 windows and not the low OH^- quartz windows. Although disturbing at first, this result is to be expected noting the huge impact the quartz windows had on improving output energy. Since the ability to lase is much stronger with the quartz windows, it is likely that the AOM device, while acceptable in the higher loss situation, could not provide sufficient loss modulation to narrow the modes lasing. Although it is true that the quartz window equipped laser may have greater access to the wings of the gain bandwidth, it is easy to picture that a wider circulating pulse (in the time domain) could pass through the modulator because of the lack of sufficient modulation intensity. Presented another way, the laser equipped with quartz windows could lase easily on a simple glass wedge output coupler while the CaF_2 equipped laser could not. Therefore, the improved quartz window laser needed an AOM operating at a greater diffraction efficiency, to achieve the same or better results for minimum pulse width.

BROADENING MECHANISM

Working with low gas pressure, one would expect that redistribution of the usable gain would be slow in comparison to the speed of its extraction by lasing during the cavity buildup time. This is certainly the case and is historically labeled inhomogenous or Doppler broadening of the gain. The question now is whether or not the validity of inhomogenous broadening and its impact on the minimum pulse width [2.6-7] extends

through the data points from 1 Torr out to 30 Torr. According to [44], up to 30 mbar (22.6 Torr), the gain spectrum is broadened via Doppler Broadening [45] through

$$\Delta\nu_{doppler} = \frac{2}{\lambda_o}\sqrt{\frac{2kT\ln 2}{M}} \qquad [4.3\text{-}1]$$

where λ_o = Wavelength at Line Center
k = Boltzman Constant
T = Temperature in °K
M = Molecular Weight of Radiating Particle (127kg / kmol for I*)

where $\Delta\nu_{doppler}$ is the FWHM in Hz of the gas evaluated at line center of λ_o. When collisions impact more strongly on the broadening of the gain, the medium is said to be homogeneously or collisionally broadened. The line width is then determined by a Lorenztian line shape which has its FWHM at [46]

$$\Delta\nu_{collision} = \frac{NQ}{\pi}\sqrt{\frac{16kT}{\pi M}} \qquad [4.3\text{-}2]$$

where Q = Collision Cross Section
N = # Atoms / m^3

From [47] and [48] it is known that CF_3I contributes 11.3 MHz/Torr while I* contributes 16 MHz/Torr to pressure broadening. Within the confines of the gain cell, these values of pressure broadening coefficients combined with the mole fraction of the respective species dominate the total pressure broadening. The actual calculation shows that in the range of 18-22 Torr, the broadening mechanisms compete equally. Homogeneous and in-homogeneous broadening is intimately connected to the previously derived (Section 2.6) minimum pulse widths for active mode locking. Since the transition between the two

occurs within the pressure range of data points the properties of both will be apparent.

First of all, focus attention to the part of the Figures 4-13 and 4-14 from 22 to 30 Torr. In this range, pulse width is decreasing. The effects of homogenous broadening are beginning to manifest themselves. From [2.6-7] this qualitative decrease would be expected. The central lasing lines are starting the collisional communication process and are supporting modes that are not necessarily above threshold but that do help to decrease pulse width. To apply [2.6-7] here to compare the experimental results would be unwise because the pressure broadening effects do not dominate in this region.

Secondly, in the range from 10 to 20 Torr, the pulse width is undergoing a characteristic dip with a minimum near the optimum energy output pressure. In this region, the Voigt line shape must be used to determine the gain bandwidth. The effects of [2.6-7] and 2.6-8 are competing equally. Currently, the shape of the minimum pulse width is a consistent part of the data but remains unexplained.

Thirdly, in the range from 10 to 4 Torr, the minimum pulsewidth is decreasing. This behavior is unexpected. From 2.6-8 it would be predicted that the pulse width would level off to a set value that is determined mainly by the Doppler bandwidth of 250 MHz. One explanation for this contradiction is that the gain bandwidth is much wider than thought allowing more longitudinal modes to exist under the gain bandwidth and hence a more narrow than predicted pulse width. The next section will approach this topic in detail. At 4 Torr, however, a comparison of the theory and experiment is in order because [2.6-7] should hold. With a gain bandwidth of 295 MHz (250 MHz, due to Doppler broadening and 45 MHz, due to pressure broadening), the predicted minimum pulse width is 1.7 ns, while the measured minimum is 1.8 ns.

KINETIC ENERGY CONTRIBUTION TO VELOCITY DISTRIBUTION

The process of photolysis in this laser system, [2.3-1], is the absorption of a UV

photon by CF_3I. After this absorption, the products are left with a considerable amount of excess energy in the form of kinetic energy. It is this kinetic energy that can disturb the Doppler distribution of velocities and leave the inverted population with a skewed velocity profile. The question then arises: "How is the gain distributed during the time that a laser pulse builds up and has access to that gain?" If the pressure inside the cell is high, one would expect that collisional processes would restore the velocity distribution back to Doppler in a time period less than the cavity buildup time. In this laser system, the overall pressure is very low and collisional processes cannot quickly restore the population to a Maxwellian distribution. To get an idea of how quickly the velocity profile does change, a recent paper by Cline, Taatjes, and Leone [49] on nascent velocity profiles of photo fragmented I^* is useful. In their paper, the photo fragmented velocity profiles of I* returned to a Maxwellian distribution within 5 μs at 17 Pascal (0.1 Torr). At 4 Torr then, it is reasonable to assume that a circulating pulse may have access to a much broader gain profile during a nominal cavity buildup time of 200-600 ns. Unfortunately, the probe signal in this experiment was not of sufficient power to allow utilizationa of a high speed detector to determine the approximate time to return to a Maxwellian velocity profile. So, given the slow speed measurements of the gain versus time, it cannot be concluded that this mode locked laser has access to an increased gain bandwidth during its cavity buildup time.

5. CONCLUSION

A longitudinally pumped photolytic iodine laser using CF_3I as a gain medium and operating at a wavelength of 1.315 μm has been acousto-optically mode locked at a pressure range of 2 to 30 Torr.

Characterization of this system, prior to mode-locking, showed it to be an efficient and powerful laser. Energy extraction efficiency was measured at 21%. The maximum energy and power recorded were 5.7 mJ and 15.5 kW respectively. Small signal gain was measured on the strongest hyperfine transition (3-4) with a sophisticated diode source of IR light. The peak value of gain was measured at 3.8 %/cm. Indirect measurements of gain confirmed this result.

Once the optimal laser parameters were established, the device was mode locked with an acousto-optic device. Studies of minimum pulse width versus pressure were undertaken. The minimum pulse width measured was 1.8 ns at 4 Torr which is in good agreement with the predicted value of 1.7 ns due to inhomogeneous broadening of the gain.

6. FUTURE WORK

DOUBLE PULSING

One interesting aspect of studying low pressure atomic iodine, is the possibility of lasing from two or more hyperfine allowed transitions. It is known that as pressure decreases, state mixing via collisions is reduced. This collisional reduction could translate into reduced "communication" between levels within the fine structure $5^2P_{1/2}$ and $5^2P_{3/2}$. as compared to the speed of the radiative processes. In theory then, population could be dumped out of the upper state into the ground state through the weaker transition 2-2 before collisional energy transfers could equilibrate energy back into the 3-4 transition for it to lase. Restated, the stimulated emission field could drive population out of one transition 3-4, and the 2-2 transition (if above threshold) could also lase before shifting its energy, through collisions, back to the F-3 hyperfine level. This type of effect has been observed during a significant portion of the mode locking experiments and I feel obligated to discuss the attempts to quantify it.

Some [50] have proposed a simplified model to examine the process and predict multi-pulse occurrence. The model assumes the levels behave as in Figure 6-1. The ground state is lumped into one level because of the rapid nature of mixing there. Efficiency of mixing in the lower level is independent of the type of perturbing particle [51] and is due to Van Der Waals interaction [52] and is therefore very fast. The upper level, on the other hand, experiences a lesser mixing rate. This is due, in part, because for electrostatic collisions the upper level the probability of a transition within the hyperfine

level is zero in the first order perturbation, due to Krammer's rule [53]. This leaves resonant energy transfers with ground state iodine atoms as the

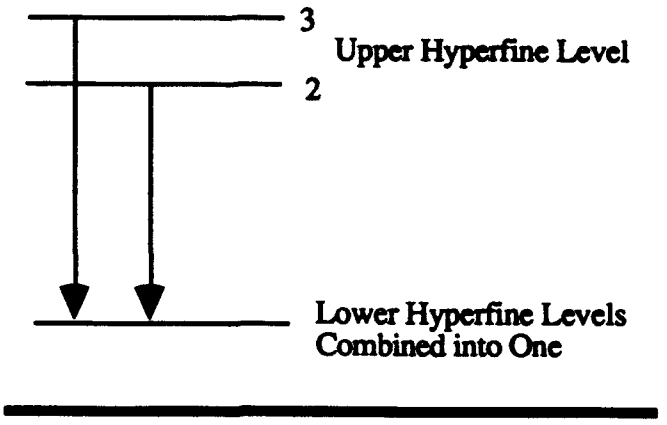

Figure 6-1 "Three Level Model"

main cause of mixing. In all, under typical conditions, the mixing in the lower hyperfine levels is much greater than the mixing in the upper hyperfine levels. Figure 6-1 can be used to aid in modeling the multiple pulse effect.

A rate equation model [54] modified for longitudinal operation and whose state mixing is built upon Figure 6-1 predicts double pulsing under various conditions. A computer simulation (Figure 6-2), near lab conditions to be used in section 4.5, shows the onset of discernible double pulsing.

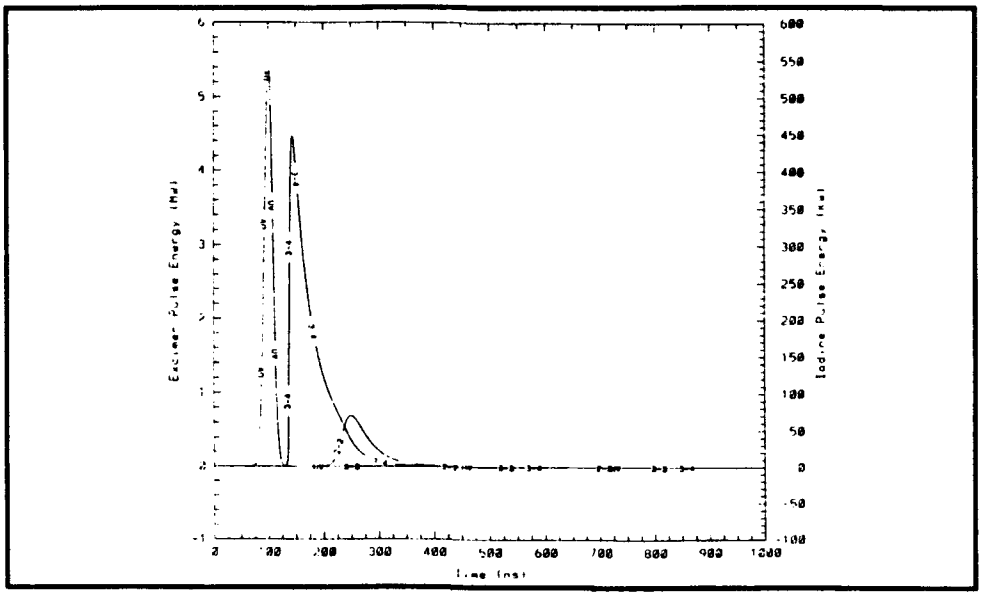

Figure 6-2 "Double Pulse Plot"

Other features become apparent in the coupled rate equation model not investigated by [50] in their attempt to model the multi-line lasing effect. Given the appropriate conditions under computer simulation, the 3-4 line can lase and then repeat lase before the

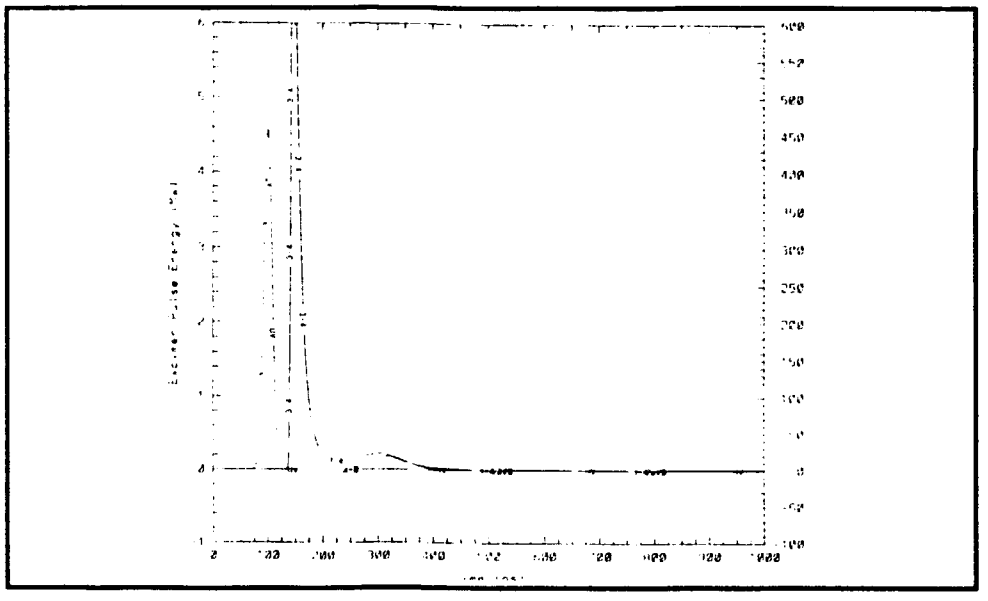

Figure 6-3 "Triple Pulse Plot"

2-2 line lases. This example, Figure 6-3 "Triple Pulse Plot", shows some interesting predicted effects in the low pressure regime.

Figure 6-4 represents a typical time-based plot of output energy for a shortened cavity. These type of measurements were taken after the mode locking experiments were completed due to the considerable damage the rear optic would suffer. The structure that occurs within the first few microseconds is assumed to be some type of multi-line lasing effect. Beyond that time frame, few explanations are yet available.

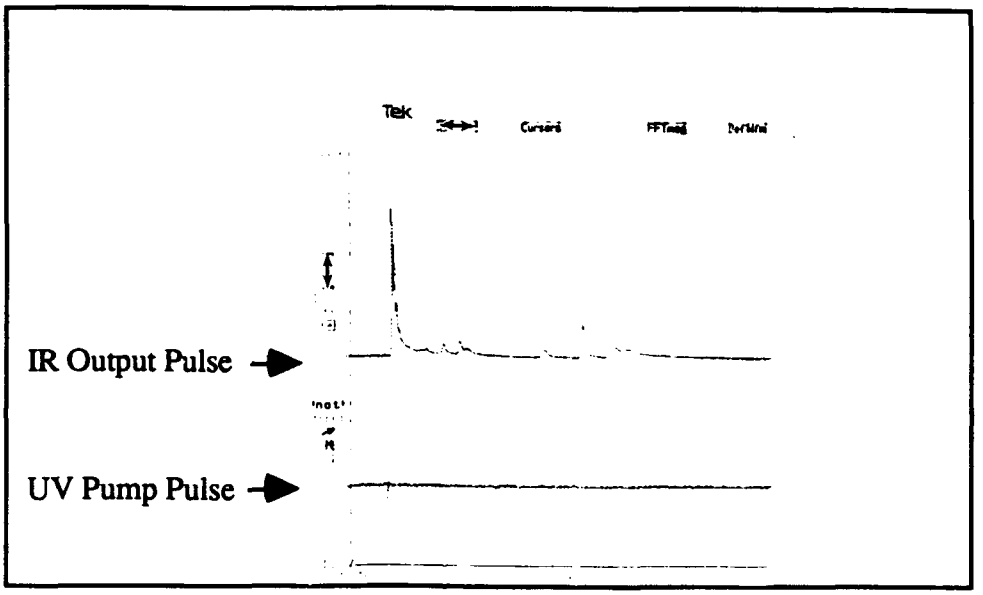

Figure 6-4 "Multi-Pulse Lasing"

FUTURE WORK

Two experiments come to mind that could answer some sticky questions raised by this experiment. First of all, a time and spectral based analysis of the above multi-line effect could clear up whether or not lasing is coming from only the strongest transition (3-4) or possibly other transitions (2-2, etc.). The long time frame (>5 μs) multiple relasing could be due to some type of recombination process in the lower hyperfine level.

Consistent repeatable data could be used here to match the rate equation computer model to derive solid answers.

The second experiment would involve the accurate measurement of the time based gain with a faster detection system. This data could define whether or not a mode locked laser, at these low pressures, has access to an increased bandwidth (during cavity build up time) and hence the possibility of more narrow than predicted pulses.

7. REFERENCES

[1] W. Theme and KE. Fill, "Hyperfine relaxation in the iodine photodissociation laser," *Optics Communications*, Vol. 36, No. 5, Mar. (1981), p. 2037.

[2] G. Brederlow, E. Fill, K.J. Witte, "The High-Power Iodine Laser". *Opt Sciences*, New York (1983), p. 1.

[3] G. Brederlow, E. Fill, K.J. Witte, p. 20.

[4] G. Brederlow, E. Fill, K.J. Witte, p. 23.

[5] S. Han, J.H. Lee, *Optics Comm*, 70, 4, (1989), p. 341-344.

[6] Y.S. Kim and S.S. Lee, *Review of Scientific Instruments*, 56, 1985, p. 208-210.

[7] M.A. Kelly, *Zeeman Spectroscopy of Photolytically Pumped Atomic Iodine*, The University of New Mexico, Albuquerque (1989).

[8] J.D. Jackson, *Classical Electrodynamics*, 2nd ed., Jonh Wiley and Sons, New York (1975), chp 3, 16.

[9] M.A. Kelly, *Zeeman Spectroscopy of Photolytically Pumped Atomic Iodine*, The

University of New Mexico, Albuquerque (1989), pp. 160-162.

[10] B.W. Shore and D.H. Menzel, *Principles of Atomic Spectra*, John Wiley and Sons, Inc., New York (1968), p. 436.

[11] M.A. Kelly, *Zeeman Spectroscopy of Photolytically Pumped Atomic Iodine*, The University of New Mexico, Albuquerque (1989), pp. 197, 204.

[12] J.K. Krug and K.J. Witte, "Physical and Chemical Substances related to the atomic iodine laser," Max-Plank-Institut Fur Quantenoptic M.P. Q. 61, (1982), p. 4.

[13] B.S. Hunt, *Parametric Studies on a Short Pulsed KrF Pumped Atomic Iodine Laser*, The University of New Mexico, Albuquerque (1993), pp. 38.

[14] B.S. Hunt, *Parametric Studies on a Short Pulsed KrF Pumped Atomic Iodine Laser*, The University of New Mexico, Albuquerque (1993), 143.

[15] A.E. Siegman, *Lasers*, University Science Books, Mill Valley CA (1986), p. 1045.

[16] A.E. Siegman, p. 1046.

[17] A.E. Siegman, p. 1050.

[18] L. Brillouin, *Annales de Physique 17*, 88 (1921).

[19] A. Korpel, *Acousto-Optics*, Marcel Dekker, Inc., New York, 1988, p. 8.

[20] P. Debye and F.W. Sears, *Proc. of the National Academy of Sciences* 18(6), 409 (1932).

[21] R. Lucas and P. Biquard, *Journal de Physique* 7(10), 464 (1932).

[22] A. Korpel, *Acousto-Optics*, Marcel Dekker, Inc., New York, 1988, p. 10.

[23] A. Korpel, p. 11.

[24] C. Raman and N. Nath, *Proc. of the Indian Academy of Sciences* 2, 406 and 413 (1935); 3, 75, 119, and 459 (1936).

[25] T.V. Higgins, "A-O Modulation", *Laser Focus World*, p. 134.

[26] IntraAction Corp., Acoustic-Optiac Manual for Model ML-503QW1, p. 2.

[27] A. Korpel, *Acousto-Optics*, Marcel Dekker, Inc., New York, 1988, p. 283.

[28] T.V. Higgins, "A-O Modulation", *Laser Focus World*, p. 136.

[29] E. Gordon, *Appl. Optics* 5, (1966), 1629.

[30] R. Dixon, *J. of Appl. Phys* , 38, (1967), 3634.

[31] T.V. Higgins, "A-O Modulation", *Laser Focus World*, p. 140.

[32] T.V. Higgins, "A-O Modulation", *Laser Focus World*, p. 160.

[33] A.E. Siegman, *Lasers*, University Science Books, Mill Valley CA (1986), p. 1065.

[34] A.E. Siegman, p. 1076.

[35] A.E. Siegman, p. 1064.

[36] A.E. Siegman, p. 1065.

[37] A.E. Siegman, p. 1067.

[38] A.E. Siegman, p. 1068.

[39] A.E. Siegman, p. 1059.

[40] IntraAction Corp., Acoustic-Optiac Manual for Model ML-503QW1, p. 5.

[41] IntraAction Corp., Acoustic-Optiac Manual for Model ML-503QW1, p. 6.

[42] H. Weichel and L.S. Pedrotti, *Electro-Optical Systems Design (EOSD) Handout*, Department of Physics, AFIT, Wright-Patterson AFB, Ohio.

[43] H. Weichel and L.S. Pedrotti, *Electro-Optical Systems Design (EOSD) Handout*, Department of Physics, AFIT, Wright-Patterson AFB, Ohio.

[44] G. Brederlow, E. Fill, K.J. Witte, "The High-Power Iodine Laser". *Opt Sciences*, New York (1983), p. 8.

[45] H. Weichel and L.S. Pedrotti, *Electro-Optical Systems Design (EOSD) Handout*, Department of Physics, AFIT, Wright-Patterson AFB, Ohio.

[46] H. Weichel and L.S. Pedrotti, *Electro-Optical Systems Design (EOSD) Handout*, Department of Physics, AFIT, Wright-Patterson AFB, Ohio.

[47] J.K.G. Krug and K.J. Witte "Physical and Chemical Data of Substances Related to the Atomic Iodine Laser". *Max-Planck-Instutut Fur Quantenoptik*, Germany(1982), p. 7.

[48] G. Brederlow, E. Fill, K.J. Witte, "The High-Power Iodine Laser". *Opt Sciences*, New York (1983), p. 12.

[49] C.A. Taatjes, J.I. Cline, and S.R. Leone, "A general method for Doppler determination of ..". J. Chem. Phys. 93(9), (1990).

[50] V.A. Alekseev, T.L. Andreeva, V.N. Volkov, and E.A. Yukov, "Kinetics of the Generation Spectrum of a Photodissociation Iodine Laser", *Soviet Physics JETP*, Vol. 36, No. 2, Feb(1989), pp. 238-242.

[51] E.A. Yukov, "Elementary processes in the active medium of an iodine photo dissociation laser", *Soviet Journal of Quantum Electronics*, Vol. 3, No 2, Sep. (1973), pp. 117.

[52] A.I. Ikunevich and V.I. Perel, *Soviet Physics JETP*, 31, 1970, p. 356.

[53] L.D. Landau and E. M. Lifshitz, *Quantum Mechanics*, Addison-Wesley, 1965.

[54] B.S. Hunt, *Parametric Studies on a Short Pulsed KrF Pumped Atomic Iodine Laser*, The University of New Mexico, Albuquerque (1993), 143.

8. APPENDIX

8.1 Hyperfine Population Rate Equations

$$\frac{d[I_3^{upper}]}{dt} = \frac{7}{12} f(I^*) W_{I^*}(t) + k_{23}^{upper}[I_2^{upper}][M_{upper}] - k_{32}^{upper}[I_3^{upper}][M_{upper}] - (A_{34} + A_{33} + A_{32})[I_3^{upper}]$$

Pump term Relaxation Terms Spont. Transtion Terms

$$-\sigma_{34}\left([I_3^{upper}] - \frac{7}{9}[I_4^{upper}]\right)\frac{\bar{I}_{34}(t)}{h\nu_{34}} - \sigma_{34}\left([I_3^{upper}] - [I_3^{lower}]\right)\frac{\bar{I}_{33}(t)}{h\nu_{33}} - \sigma_{32}\left([I_3^{upper}] - \frac{7}{5}[I_2^{lower}]\right)\frac{\bar{I}_{32}(t)}{h\nu_{32}}$$

Stimulated Transition Terms

$$-[I_3^{upper}]\sum_q (k_q[M_q])$$

Quenching Terms

$$\frac{d[I_2^{upper}]}{dt} = \frac{5}{12} f(I^*) W_{I^*}(t) + k_{32}^{upper}[I_3^{upper}][M_{upper}] - k_{23}^{upper}[I_2^{upper}][M_{upper}] - (A_{23} + A_{22} + A_{21})[I_2^{upper}]$$

Pump term xation Terms Spont.Transition Terms

$$-\sigma_{23}\left([I_2^{upper}] - \frac{7}{9}[I_3^{lower}]\right)\frac{\bar{I}_{23}(t)}{h\nu_{23}} - \sigma_{22}\left([I_2^{upper}] - [I_2^{lower}]\right)\frac{\bar{I}_{22}(t)}{h\nu_{22}} - \sigma_{21}\left([I_2^{upper}] - \frac{7}{5}[I_1^{lower}]\right)\frac{\bar{I}_{21}(t)}{h\nu_{21}}$$

Stimulated Transition Terms

$$-[I_3^{upper}]\sum_q (k_q[M_q])$$

Quenching Terms

$$\frac{d[I_4^{lower}]}{dt} = \frac{9}{24}\left(1 - f(I^*)\right)W_{I^*}(t) + k_{34}^{lower}[I_3^{lower}][M_{lower}] + k_{24}^{lower}[I_2^{lower}][M_{lower}] + k_{14}^{lower}[I_1^{lower}][M_{lower}]$$

Pump term — Relaxation Terms

$$- \left(k_{43} + k_{42} + k_{41}\right)[I_4^{lower}][M_{lower}] - \sigma_{34}\left([I_3^{upper}] - \frac{7}{5}[I_4^{lower}]\right)\frac{\bar{I}_{34}(t)}{h\nu_{34}} + A_{34}[I_3^{upper}]$$

Relaxation Terms — Stimulated Transition Terms — Spon. Transition Term

$$+ \frac{9}{24}\left([I_3^{upper}] + [I_2^{lower}]\right)\sum_q\left(k_q[M_q]\right) - k_R[I_4^{upper}][CF_3] - [I_4^{lower}]^2\sum_i\left(k_i[M_i]\right)$$

Quenching Terms — Recombination and Dimerization Terms

$$\frac{d[I_3^{lower}]}{dt} = \frac{7}{24}\left(1 - f(I^*)\right)W_{I^*}(t) + k_{43}^{lower}[I_4^{lower}][M_{lower}] + k_{23}^{lower}[I_2^{lower}][M_{lower}] + k_{13}^{lower}[I_1^{lower}][M_{lower}]$$

Pump term — Relaxation Terms

$$-\left(k_{34} + k_{32} + k_{31}\right)[I_3^{lower}][M_{lower}] + \sigma_{33}\left([I_3^{upper}] - [I_3^{lower}]\right)\frac{\bar{I}_{33}(t)}{h\nu_{33}} + \sigma_{23}\left([I_2^{upper}] - \frac{5}{7}[I_3^{lower}]\right)\frac{\bar{I}_{23}(t)}{h\nu_{23}}$$

Relaxation Terms — Stimulated Transition Terms

$$+ A_{33}[I_3^{upper}] + A_{23}[I_2^{upper}] + \frac{7}{24}\left([I_3^{upper}] + [I_2^{upper}]\right)\sum_q\left(k_q[M_q]\right)$$

Spon. Transition Term — Quenching Terms

$$- k_R[I_3^{lower}][CF_3] - [I_3^{lower}]^2\sum_i\left(k_i[M_i]\right)$$

Recombination and Dimerization Terms

$$\frac{d[I_2^{lower}]}{dt} = \frac{5}{24}\left(1 - f(I^*)\right)W_{I^*}(t) + k_{42}^{lower}[I_4^{lower}][M_{lower}] + k_{32}^{lower}[I_3^{lower}][M_{lower}] + k_{12}^{lower}[I_1^{lower}][M_{lower}]$$

Pump term **Relaxation Terms**

$$-\left(k_{24} + k_{23} + k_{21}\right)[I_2^{lower}][M_{lower}] + \sigma_{32}\left([I_3^{upper}] - \frac{7}{5}[I_3^{lower}]\right)\frac{\bar{I}_{32}(t)}{h\nu_{32}} + \sigma_{22}\left([I_2^{upper}] - [I_2^{lower}]\right)\frac{\bar{I}_{22}(t)}{h\nu_{22}}$$

Relaxation Terms **Stimulated Transition Terms**

$$+ \quad A_{32}[I_3^{upper}] \quad + \quad A_{22}[I_2^{upper}] \quad + \quad \frac{5}{24}\left([I^{upper}]\right)\sum_q\left(k_q[M_q]\right)$$

Spon. Transition Term **Quenching Terms**

$$- \quad k_R[I_2^{lower}][CF_3] \quad - \quad [I_2^{lower}]^2\sum_i\left(k_i[M_i]\right)$$

Recombination and Dimerization Terms

$$\frac{d[I_1^{lower}]}{dt} = \frac{3}{24}\left(1 - f(I^*)\right)W_{I^*}(t) + k_{41}^{lower}[I_4^{lower}][M_{lower}] + k_{31}^{lower}[I_3^{lower}][M_{lower}] + k_{21}^{lower}[I_2^{lower}][M_{lower}]$$

Pump term **Relaxation Terms**

$$- \quad \left(k_{14} + k_{13} + k_{12}\right)[I_1^{lower}][M_{lower}] \quad + \quad \sigma_{21}\left([I_2^{upper}] - \frac{5}{3}[I_1^{lower}]\right)\frac{\bar{I}_{21}(t)}{h\nu_{21}}$$

Relaxation Terms **Stimulated Transition Terms**

$$+ \quad A_{21}[I_2^{upper}] \quad + \quad \frac{3}{24}\left([I^{upper}]\right)\sum_q\left(k_q[M_q]\right)$$

Spon. Transition Term **Quenching Terms**

$$- \quad k_R[I_1^{lower}][CF_3] \quad - \quad [I_1^{lower}]^2\sum_i\left(k_i[M_i]\right)$$

Recombination and Dimerization Terms

8.2 Two-Way Circulating Intensity Rate Equations

$$\frac{d\bar{I}_{34}(t)}{dt} = \sigma_{34}\left([I_3^{upper}] - \frac{7}{9}[I_4^{lower}]\right)\frac{L_g c}{d}\bar{I}_{34}(t) - \gamma_{--}\bar{I}_{34}(t) + 2Q\frac{L_g}{d}$$

$$\frac{d\bar{I}_{33}(t)}{dt} = \sigma_{33}\left([I_3^{upper}] - [I_3^{lower}]\right)\frac{L_g c}{d}\bar{I}_{33}(t) - \gamma_{--}\bar{I}_{33}(t) + 2Q\frac{L_g}{d}$$

$$\frac{d\bar{I}_{32}(t)}{dt} = \sigma_{32}\left([I_3^{upper}] - \frac{7}{5}[I_2^{lower}]\right)\frac{L_g c}{d}\bar{I}_{32}(t) - \gamma_{--}\bar{I}_{32}(t) + 2Q\frac{L_g}{d}$$

$$\frac{d\bar{I}_{23}(t)}{dt} = \sigma_{23}\left([I_3^{upper}] - \frac{5}{7}[I_3^{lower}]\right)\frac{L_g c}{d}\bar{I}_{23}(t) - \gamma_{--}\bar{I}_{23}(t) + 2Q\frac{L_g}{d}$$

$$\frac{d\bar{I}_{22}(t)}{dt} = \sigma_{22}\left([I_2^{upper}] - [I_2^{lower}]\right)\frac{L_g c}{d}\bar{I}_{22}(t) - \gamma_{--}\bar{I}_{22}(t) + 2Q\frac{L_g}{d}$$

$$\frac{d\bar{I}_{21}(t)}{dt} = \sigma_{21}\left([I_3^{upper}] - \frac{5}{3}[I_3^{lower}]\right)\frac{L_g c}{d}\bar{I}_{21}(t) - \gamma_{--}\bar{I}_{21}(t) + 2Q\frac{L_g}{d}$$